University of Alberta

OPTICAL PROPERTIES OF SILICON-NANOCRYSTAL COATED MICROSPHERES

by

Angela Melina Beltaos 

A thesis submitted to the Faculty of Graduate Studies and Research
in partial fulfillment of the requirements for the degree of
Master of Science

Department of Physics
Edmonton, Alberta
Spring, 2006

Your file Votre référence
ISBN: 0-494-13790-8
Our file Notre référence
ISBN: 0-494-13790-8

Dedicated to my family: Spyros, Ljilja, Terry, Elaine, and Andrew Beltaos.

ABSTRACT

The luminescence of silicon nanocrystals can be coupled to optical microcavity modes in order to control many aspects of the emission, such as the directionality, spectral intensity, and lifetime. Spherical microcavities made from silica or polymers can be particularly efficient in trapping light and hence display strong resonant optical modes. In this research a method has been developed for coupling the luminescence of silicon nanocrystals into silica microspheres by coating the spheres with a nanocrystal film. The resulting emission spectra of these structures showed strong optical cavity modes. Effects of sphere size, film thickness, and emission location within the sphere on the emission spectra were investigated.

ACKNOWLEDGEMENTS

Many thanks to all those who have assisted me with this work:

My supervisor, Al Meldrum, for his guidance throughout my time working with him. and his helpful comments and editing for this thesis.

My colleagues, Cindy Blois, Megan Glover, Aaron Hryciw, and Nicole MacDonald, for helpful discussions and lab assistance. Special thanks to Aaron also for help with Matlab programming.

Ken Marsh, Don Mullin, and Greg Popowich of the Physics Department for lab assistance.

Philip Laven of the European Broadcasting Union, for helpful correspondence and for the update to his program Mieplot to subtract the background of spectra.

George Braybrook of the Department of Earth and Atmospheric Sciences, for the SEM photos.

Jon Veinot of the Chemistry Department for showing me how to make sphere arrays, and for the use of his lab space and materials for drop-coating spheres.

Zbigniew Gortel of the Physics Department for helpful discussions during committee meetings.

My family for their advice, encouragement, and help: Ljilja for her editing; Elaine and Andrew for LaTeX assistance; Spyros and Terry for helpful discussions.

Hongtao Yang, who wrote the LaTeX style file mathesis.sty that I used for this thesis.

The Department of Physics and the Province of Alberta for financial support.

Table of Contents

List of Figures

List of Tables

Chapter 1

Introduction

For several decades, silicon (Si) has been the most technologically important semiconductor due to its excellent electronic and mechanical properties, and because of the ease and low cost associated with its production. However, owing to its indirect bandgap, it is a poor light emitter and hence has had limited potential in optoelectronics applications. Researchers have searched for ways to overcome this difficulty - for example, under careful synthesis conditions in which bulk crystalline silicon wafers are textured, the light emission quantum efficiency can be up to 10.2% [79]. Silicon nanocrystals currently represent one particularly attractive possibility for making luminescent silicon. Since the discovery of room-temperature photoluminescence (PL) from porous silicon in 1990 [12], researchers have identified numerous standard thin film and ion implantation methods that result in films of luminescent silicon nanocrystals embedded in a matrix of SiO_2 (eg. see [43, 29, 75, 60]). However, although test devices such as light emitting diodes (LEDs) have been demonstrated using Si nanocrystals [4], significant challenges must be overcome before the technological potential of these materials will be realized. For many applications the luminescence is broad, has low quantum efficiency and is difficult to tune.

By embedding Si nanocrystals inside planar microcavities, these problems can be at least partly overcome. Fabry-Perot microcavities have characteristic resonance wavelengths into which the luminescence can couple, thereby narrowing the emission linewidth, increasing the intensity in the direction of confinement, and possibly altering the radiative rates [39, 65, 78, 36]. For example, Iacona et al. [39] grew a silicon nanocrystal layer sandwiched between a pair of distributed Bragg reflectors

(DBRs) to produce resonant wavelengths centered between 700 and 950 nm, with an optical quality factor (Q factor) of 500. Using metal mirrors to sandwich amorphous silicon nanocrystals, Hryciw et al. [36] tuned the photoluminescence wavelength between 480 and 900 nm with a Q factor of approximately 100.

Planar cavities, although relatively easy to synthesize, result in only one dimensional optical confinement and can be limited by the presence of waveguide modes in the plane of the cavity. In contrast, three dimensional microcavities can offer "complete" confinement due to the lack of any non-confined modes, resulting in much stronger coupling of the PL to the cavity modes. The most obvious candidate for a three-dimensional microcavity is the high index sphere or droplet in which the PL is enhanced due to total internal reflection inside the sphere [41]. Spherical microcavities have been investigated by many researchers and are among the most attractive candidates for experiments in cavity quantum electrodynamics due to the very high Q factors that can be obtained [31, 1, 7].

The basic physics of the dielectric microsphere is a result of total internal reflection as photons "orbit" at the edges of the sphere. The light is trapped into the so-called "Whispering Gallery Modes" (WGMs) of the sphere, and the resulting Q factors can be much higher than those that can be achieved in planar cavities [7]. Although there have been several studies coupling the PL from II-VI semiconductor nanocrystals into the cavity modes of microspheres (eg. see [10, 47, 7, 5]), so far there have not been many studies using Si nanocrystals. Attempts to incorporate Si nanocrystals into silica (SiO_2) microspheres have previously been made; however, during the processing steps (ion implantation of silicon into the microspheres) the spheres were deformed to the degree that the WGMs were virtually non-existent in the PL spectra [70, 82].

In this thesis research, a new and simple method of incorporating Si nanocrystals onto SiO_2 microspheres has been developed. This particular method allowed us to achieve strong WGMs in the PL spectra and to obtain higher Q factors than possible in planar cavities. The basis of this method is that SiO_2 spheres are coated with a thin layer of silicon-rich oxide which, upon annealing, segregates into a layer of silicon nanocrystals embedded in SiO_2 that sits directly on top of the microspheres. After proving that the method could work in principle, the main goals of the research were addressed: to couple the PL from the nanocrystals into the

WGMs of the microspheres, to obtain higher Q factors than previously reported for planar microcavities, to control the PL using different microsphere sizes and different thicknesses of the nanocrystal film, to estimate the Q factors possible with this method, to produce long-range two dimensional luminescent microsphere arrays, and to suggest future means to improve the Q factors for silicon nanocrystals in spherical microcavities.

The structure of this thesis is arranged as follows: Chapter 2 reviews the basic physics behind the photoluminescence of silicon nanocrystals and introduces the relevant theoretical basis for the behavior of light trapped inside spherical microcavities. As well, a review of previous microsphere/nanocrystal work by other research groups is given. Chapter 3 outlines the experimental set-up and the experiments performed for this thesis including details of materials used. In Chapter 4 the results of the experiments are presented through microscope images and PL spectra. The physical meaning of these results are discussed. Analysis of the spectra and a comparison of the experimental results to theoretical predictions is given in Chapter 5. Finally, Chapter 6 summarizes the results of this thesis and discusses future research directions.

Chapter 2

Background

2.1 Silicon Nanocrystals

2.1.1 General Background: Semiconductor Nanocrystals

Semiconductor nanocrystals are small clusters of semiconductor material consisting of hundreds to several thousands of atoms. Due to their size, they have a mix of the properties of the bulk material and properties of a single atom [46]. They are small enough to exhibit quantum confinement effects in their electronic structure, while large enough to have a crystal structure that is the same as that of the bulk phase [3]. Nanocrystals are often referred to as artificial atoms or quantum dots (QDs) since quantum confinement effects lead to atomic-like discrete electronic states. This causes a QD to have an absorption spectrum made up of discrete lines, unlike the bulk semiconductor. In general, the optical and electronic properties of a QD are strongly size-dependent, and are much different than those of the same material in bulk form [46].

The range of sizes over which quantum effects become important is determined primarily by the effective masses of electrons and holes and by the dielectric constant of the semiconductor. A variety of theoretical approaches has been taken to calculate how the bandgap and density of states changes as a function of particle size, and the theoretical results match closely with experiment [24, 32, 33, 87, 21, 22, 64]. For example, by reducing the diameter of cadmium selenide (CdSe) nanocrystals from 200 Å to 20 Å, the bandgap is observed to change from 1.7 eV to 2.4 eV, while the colour of luminescence changes from deep red to green [3]. This increase in bandgap

with reduction of particle size is a relationship that has been well explained by theory [24].

A simple estimation of the effects that occur in semiconductor nanocrystals can be obtained from the so-called effective mass approximation (EMA). Although this ignores many of the complicating factors such as non-parabolicity of the valence band, spin-orbit interactions, and other effects that more complete theories can take into account [32, 33, 87, 21, 22, 64], it does provide a simple, semi-quantitative picture describing the shifting of the energy levels as a function of size and the selection rules associated with different possible transitions.

In the EMA, electrons and holes in a nanocrystal are assumed to have the same effective masses as in an ideal bulk crystal with the same stoichiometry [26]. The spatial separation of the electron and hole in the QD is given by the *exciton Bohr radius* [62]:

$$r = \frac{\epsilon h^2}{\pi m_r e^2} \tag{2.1}$$

where r is the radius of a sphere defined by the separation of the electron and hole in three dimensions, ϵ is the dielectric constant of the material, h is Planck's constant, m_r is the reduced mass of the electron-hole pair, and e is the charge of an electron.

When semiconductor particles have a radius of less than the exciton Bohr radius (~1 - 10 nm for most semiconductors, and ~5 nm for Si), they are said to be in the strong quantum confinement regime [59]. At this size scale, spatial confinement in all directions causes electrons and holes to "feel" the presence of particle boundaries. The wavefunctions inside a spherical particle with high potential barriers are much like the familiar particle-in-a-box problem of quantum mechanics. As the particle size decreases, the valence and conduction bands are discretized and the energy of the lowest states for electrons (holes) in the conduction (valence) band increases. In the EMA approximation, the energy of the bandgap in a semiconductor QD is given by [62]:

$$E_g(QD) = E_g(bulk) + \frac{h^2}{8R^2}\left(\frac{1}{m_e} + \frac{1}{m_h}\right) - \frac{1.8e^2}{4\pi\epsilon_0\epsilon R} \tag{2.2}$$

where E_g is the bandgap energy of the QD or bulk material, R is the radius of the QD, m_e is the effective mass of the electron, and m_h is the effective mass of the hole. In the right hand side of this equation, the middle term is due to quantum

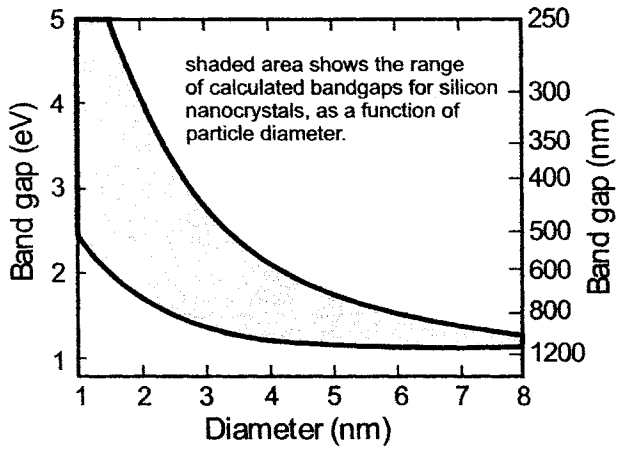

Figure 2.1: Range of theoretical calculations for the bandgap of Si nanocrystals as a function of particle size. Figure reproduced from [59] (in which it was modified from [89]).

effects, while the last term is due to the Coulomb attraction between the electron and the hole.

More specifically to this thesis, the relationship given in Equation 2.2 is often observed in silicon nanocrystals. The theoretical bandgap of Si as a function of particle size has been calculated by a number of authors [32, 33, 87, 21, 22, 64]. There is a considerable range within these predictions, but all of them show that the bandgap increases in smaller Si particles due to quantum confinement (see Figure 2.1).

In the small size regime of semiconductor nanocrystals, not only is the bandgap energy affected by the confinement, but also the density of states in the valence and conduction bands. In the bulk material, the density of states is lowest near the band edges and increases with increasing energy of the electrons and holes. However, in the nanoscale material, the density of states is highest near the band edges. Because most transitions occur from near the band edges, the range of emission energies is small, and therefore the PL spectrum has a narrow linewidth.

A full treatment of the physics of semiconductor nanostructures is beyond the scope of this thesis, so the reader is referred to Gaponenko [26] for a complete summary of the quantum size effects characteristic of nanoscale semiconductors. However, in this simplified picture it is readily apparent that the optical transitions are strongly dependent on particle size when the particles are smaller than the Bohr

exciton radius. The emission spectrum is intensified and narrowed as compared to the bulk material, making semiconductor nanocrystals attractive for light emission applications.

2.1.2 Synthesis of Silicon Nanocrystals and the PL Spectrum

Although quantum size effects have been observed for years in direct gap semiconductors, luminescence from low-dimensional silicon was not observed until the 1980s by researchers experimenting with silicon-rich thin films and porous silicon [13, 92, 68, 25]. However, at that time, they did not realize that the luminescence came from nanoscale silicon; rather, they concluded that the luminescence was due to the presence of amorphous hydrogenated silicon. It was not until 1990, in a study on porous silicon, that the observed photoluminescence was suggested to be due to quantum confinement effects in silicon nanocrystals within the porous silicon network [12]. That paper sparked an enormous amount of research interest due to the potential applications of light-emitting silicon and has been cited more than 3,600 times. Presently it is well known that silicon nanoparticles exhibit strong room temperature PL with an efficiency as high as 10,000 times greater than that of bulk silicon [52]. Although porous silicon has been widely studied, silicon nanocrystals embedded in a solid host material have more potential for applications due to their greater chemical and mechanical durability [59].

Silicon nanocrystals can be made by a number of methods including thin film physical or chemical vapour deposition, ion implantation, pulsed laser deposition, and chemical precipitation [59]. In most of these methods, a thin film of silicon rich oxide (SiO_x, where $1 < x < 2$) is deposited onto a substrate and then exposed to high temperatures (i.e. annealed). When the film is annealed at temperatures of 1000 ^oC or higher, the SiO_x film phase separates to form Si nanocrystals embedded in an SiO_2 film.

The PL spectrum from silicon nanoparticle films almost invariably peaks in the near infrared part of the spectrum between 700 - 1000 nm. As well, the spectrum is always broad, with a full-width-at-half-maximum typically on the order of 150 nm. The wide emission spectrum could be due to both homogeneous and inhomogeneous broadening effects. Example spectra are shown in Figure 2.2. These spectra come from a work by Glover and Meldrum [28] in which it was shown that the peak

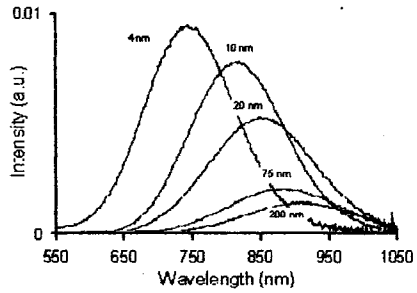

Figure 2.2: PL spectra of Si nanocrystal films of varying thicknesses (film thickness indicated next to each spectrum). Nanocrystal layers were separated by 20 nm of SiO_2. Figure reproduced from [28].

wavelength could be controlled by changing the thickness of the film in multilayer Si nanocrystal films separated by buffer layers of SiO_2.

The emission spectrum cannot be tuned to the same degree that it can for CdSe or other direct gap nanocrystals. In the latter case, the PL peak is much narrower and can be tuned right across the visible spectrum, according to the particle size. The situation is quite different for silicon nanocrystals in SiO_2 – the nanocrystal emission never peaks in the visible and the color to the eye is almost always a deep red, due to the short-wavelength tail of the spectrum. In contrast, the absorption "onset" appears in the blue part of the spectrum, and this has important implications for the photoluminescence mechanism.

2.1.3 Mechanisms of Luminescence from Silicon Nanocrystals

In bulk Si, light emission is inhibited due to its indirect bandgap. The transition of an electron from the bottom of the conduction band to the top of the valence band requires a substantial change in momentum that would not be accounted for by the small momentum of an emitted photon ($p = E/c$, where p is the photon momentum, E is the bandgap energy, and c is the speed of light). To satisfy conservation of momentum, transitions can occur only with phonon assistance, and the radiative rates in this case are very slow [3].

At a nanoscale, however, the radiative rates are greatly enhanced by confinement effects (although they are still much lower than the radiative rates of direct gap

semiconductors). The most prominent factor in the enhanced light emission in nanoscale Si is the reduction of nonradiative rates due to a geometrical effect in which nonradiative traps are isolated on individual nanoparticles [3]. The exact emission mechanism from Si nanocrystals has been greatly debated in the literature. It is a complex and interesting topic that has been studied for its own sake by many researchers. Some of the existing theories are introduced below.

The shift between the emitting and absorbing states (Stokes shift) is large (>2 eV) in silicon nanocrystals. Although many authors have proposed a direct particle size dependence of the luminescence, it is not obviously consistent with such a large Stokes shift. There can be at least two reasons for the large energy gap between the absorbing and emitting states: 1) the density of states near the band edge (i.e., ~1.5 eV) is lower by orders of magnitude compared to where the absorption onset is observed [50]. In this picture, carriers are absorbed dominantly at energies corresponding to the blue region of the spectrum, and rapidly thermalize to the band edge states in the near infrared. They subsequently recombine and produce near-IR light emission. 2) The PL is moderated by the presence of a radiative center in the bandgap. In this model, absorption occurs across the quantum-confinement-enlarged bandgap but the luminescence occurs after carriers are trapped at a radiative recombination site. [33, 38, 23, 51, 48].

Currently, the second model is gaining favor for a variety of reasons. First, López et al. [57] have used electron spin resonance methods to obtain evidence on the nature of the radiative centers and nonradiative traps. The PL intensity scales inversely with the concentration of silicon dangling bonds, consistent with the idea that the dangling bonds act as nonradiative traps. Second, there is a direct dependence between the emission energy and oxygen concentration at the nanocrystal-matrix interface [83]. Theory suggests that the Si=O double bond can trap either electrons and/or holes, and that the recombination is localized to these interface regions. Some models suggest that the energy of the radiative center tracks the bandgap energy, but is always several eV below it [93]. The Si=O double bond is thought to be the main center at work in this model since it creates a deep trap well into the bandgap [22]. This implies that the more oxygen atoms there are on the surface, the more possible recombination sites there are and statistically the smaller the emission energy will be. Hence larger nanocrystals (i.e. with more

oxygen atoms on the surface) emit at lower energies, and the experimentally observed redshift of PL from larger nanocrystals is accounted for by the radiative center model. In addition, particle interactions can strongly affect the peak PL wavelength - Glover and Meldrum [28] showed that this effect can dominate over particle size effects on the luminescence. In that work, an interactive nanocrystal model was proposed in which carriers can migrate from particle to particle, although the exact mechanism (eg. electron or exciton tunneling, dipole effects, minibands, etc.) was not determined. Energy could be transferred through closely spaced particles (less than 10 nm apart), resulting in a decrease in the overall emission energy (and a PL redshift). On the other hand, more isolated particles had less probability of carrier migration and a blueshift in the PL spectrum resulted. Hence the proximity of particles (and grain boundaries) can greatly affect the PL spectrum.

It is clear at this point that the photoluminescence mechanism is much more complex than in the case of II-VI nanocrystals. There is considerably more evidence and argument for and against a pure quantum confinement model than cited above: for example, the temperature dependence of the PL and the PL lifetimes has also been interpreted on the basis of competing models [81, 86, 11]. Based on the previous work by Glover and Meldrum [28, 27], particle size considerations alone were insufficient to account for the photoluminescence results.

2.2 Microcavities

2.2.1 General Properties of Microcavities

Much of the research in silicon nanocrystals for application purposes is directed towards making the emission spectrum sharper, more directional, more efficient, and tunable to a specific wavelength. One common method of achieving these goals is to embed Si nanocrystals in optical microcavities that trap the luminescense and intensify the emission at specific wavelengths as a result of cavity quantum electrodynamic (CQED) effects.

CQED is the study of boundary effects on electrodynamic properties of atoms inside a cavity [19]. The field must be continuous across the boundary, leading to a modification of the frequency-dependent mode density of the electromagnetic field inside the cavity [9]. The mode density for an ideal closed cavity is a series of

delta functions occurring at certain "resonance" wavelengths. If an atom inside a cavity has a transition corresponding to a resonance wavelength, it can radiate faster than in free space (this is called "enhanced spontaneous emission"). Otherwise, if the atom's transition is not at a resonance wavelength, the radiative lifetime is theoretically infinite (in a perfect cavity) and emission of light will not occur [9]. The atom will simply remain in an excited state unless it radiates into one of the "cavity modes".

There are two regimes that describe the coupling strength between the atom's transition and the cavity mode [67]. In the *weak coupling regime*, the spontaneous emission rate of an atom is enhanced inside a cavity compared to free space due to the Purcell effect (as will be defined below). In the *strong coupling regime*, spontaneous emission is a reversible process and photons that are emitted by an atom can be reabsorbed and emitted many times (known as "Rabi oscillations"). The optical properties of the system in this regime become a superposition of those of light (the photon) and matter (the atom). For the work in this thesis, the coupling strength was always in the weak coupling regime.

The *quality factor*, Q, is the measure of the optical quality of a cavity. In an ideal cavity, light would be confined indefinitely inside with no loss and the quality factor would be infinite. But in real cavities with imperfect reflectors, light escapes after a given time and the resonance peaks broaden as a result. The Q-factor is defined by the ratio of the resonance wavelength λ and bandwidth of the cavity mode $\Delta\lambda_{1/2}$ [77].

$$Q = \frac{\lambda}{\Delta\lambda_{1/2}} \tag{2.3}$$

The bandwidth $\Delta\lambda_{1/2}$ can also be referred to as the full width at half maximum (FWHM).

The higher Q is for a microcavity, the narrower the modes are and the more efficient the light trapping becomes. In fact, Q is proportional to confinement time of the light in units of the optical period [80] and can be written as

$$Q = \omega\tau \tag{2.4}$$

where $\omega = 2\pi c/\lambda$ is the optical frequency and τ is the photon lifetime in the cavity [77]. Therefore, high Q factors correspond to narrow and intense emission lines, although the overall emission intensity decreases due to the efficient trapping.

The resonant wavelengths of the cavity, λ_n, are separated by the Free Spectral Range ($\Delta\lambda_{FSR}$):

$$\Delta\lambda_{FSR} = \lambda_{n+1} - \lambda_n \tag{2.5}$$

Or equivalently, the free spectral range in terms of frequency f or any other parameter can be found by substituting that parameter with λ in the above equation.

The free spectral range changes as a function of the cavity dimensions. If the cavity is made larger, more wavelengths can resonate inside the cavity. As the size of the cavity approaches infinity (i.e. free space, in which atoms can emit at any wavelengths), $\Delta\lambda_{FSR}$ approaches zero. On the other hand, if the cavity is made smaller, the allowable wavelengths become more separated, so that $\Delta\lambda_{FSR}$ approaches infinity. A cavity with dimensions around 0.1-10 μm is ideal for isolating a few widely spaced cavity modes or even a single mode [94], as is desirable for most practical applications.

At a resonant wavelength, the intensity of light inside a microcavity is enhanced in a process known as the *Purcell Effect.* As originally reported by Purcell in 1946 [69], the density of modes per unit volume at a given transition wavelength is modified for atoms inside a cavity [80]. The density of modes is maximum at the resonant wavelengths and well below that of free space at non-resonant wavelengths, and this controls the spontaneous emission rate from the atoms inside the cavity. The more modes that are available for an atom to radiate into, the more likely spontaneous emission becomes. Therefore, spontaneous emission is enhanced at resonance wavelengths (maximum density of modes), while it is suppressed at non-resonant wavelengths (minimum density of modes). The magnitude of the enhancement is given by the *Purcell enhancement factor* [80]:

$$P = \frac{3}{4\pi^2}\left(\frac{\lambda}{N}\right)^3 \cdot \frac{Q}{V} \tag{2.6}$$

where λ is the wavelength of light, N is the refractive index of the cavity, Q is the quality factor, and V is the volume of the cavity. Note that the enhancement factor is inversely proportional to volume, showing that there is another advantage associated with the small dimensions of microcavities.

2.2.2 Planar Microcavities

In a planar cavity, the cavity modes correspond to wavelengths that exactly equal the length of the cavity when multiplied by a half-integer. In a cavity of length L with perfectly reflecting end mirrors and a refractive index of 1, the resonant wavelengths λ_n are given by [19]:

$$L = n\frac{\lambda_n}{2} \tag{2.7}$$

where n is an integer. Or equivalently,

$$\lambda_n = \frac{2L}{n} \tag{2.8}$$

Due to the simple length dependence of resonant wavelength in Equation 2.8, the wavelength of planar microcavities can be easily tuned by varying the size of the cavity [39, 36]. For example, Hryciw et al. made Fabry-Perot planar microresonators using Ag mirrors with an active layer of SRO sandwiched inside [36]. By changing the thickness of the SRO layer, the photoluminescence wavelength could be tuned between $475 - 875$ nm. As well, they developed a single graded cavity, in which the thickness of the active layer varied uniformly across a 2 inch wafer. From this one sample, all wavelengths between $475 - 875$ nm could be obtained by moving the excitation laser across the sample.

In addition to being tunable, the luminescence from planar microcavities is highly directional. Si nanocrystals embedded inside planar microcavities are known to exhibit narrow PL peaks whose intensity is more than an order of magnitude higher than similar samples in the absence of the cavity [39]. The intense, narrow, directional, and tunable emission from planar microcavities makes them very attractive for potential applications, as well as the study of cavity quantum electrodynamic (CQED) effects [49].

2.2.3 Spherical Microcavities

Although planar microcavities represent a well established technology, spherical microcavities also have recently been gaining attention for possible applications and theoretical studies. There are many differences in the emission properties of the two types of cavities arising from the different geometries. Unlike planar microcavities,

the emission from spherical microcavities is not naturally directional, and the wavelength is not easily tunable. However, a spherical cavity has one major advantage over a planar one: the cavity modes of spherical microcavities have much higher Q factors than in planar microcavities due to the three-dimensional confinement [6]. A nearly ideal spherical cavity with diameter of 5 to 10 μm can easily have Q greater than 10^5 [41], whereas recent findings of silicon nanocrystals embedded in a planar microcavity had Q factors of approximately 500 [39, 40].

In analogy with a quantum dot, a spherical microcavity is sometimes referred to as a *photonic dot* (PD) due to its three dimensional confinement of light. Using QDs in combination with PDs yields an interesting and unique structure in which both electron states of the QD and photonic states of the PD are quantized in three dimensions. Because of this property, nanocrystal-containing microspheres are attracting attention amongst both theoretical and experimental researchers. Applications of these fluorescent microspheres include the study of three-dimensional confined photon states, microlasers, and optical coding of biomolecules [31].

In the following subsections we review the important theoretical background of light inside a spherical microcavity. The equations presented in this section will later be used for comparison to the experimental results of this thesis in Chapter 5. A number of these equations (such as the resonance locations and free spectral range) were originally derived according to Mie scattering theory. Although in this case the experiment will not be dealing with light scattering from a sphere, important parts of the theory have been shown to be equivalent for emitters inside or outside the sphere (for fluorescence vs. scattering). Equivalent parts of the theory include resonance locations, linewidths and lineshapes, mode and order numbers of observable resonances, density of modes, transition rates of atoms, and the frequency dependence of these rates [34, 14, 15]. However, the angular distribution and polarization of emission from a fluorescent sphere were shown to be different from that of scattered light from the same sphere [16].

Whispering Gallery Modes

The optical cavity modes in a spherical cavity are called *Whispering Gallery Modes* (WGMs). This name originates from an acoustical effect first observed in a gallery in the Cupola of St. Paul's Cathedral in London. One can hear a whisper spoken

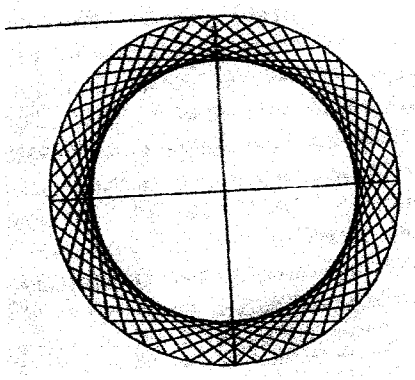

Figure 2.3: WGMs formed inside a sphere by multiple total internal reflections at the sphere-air interface. The incident light beam enters the sphere tangentially by diffraction. Figure reproduced from [34].

near the wall on the other side of the gallery (42 m away) due to the refocusing of the sound by the curved surface of the cathedral [49]. Lord Rayleigh was the first to identify this effect about 100 years ago and suggest the existence of the gallery modes. He related the idea to light as well, saying that a similar strong confinement of electromagnetic fields would be useful for applications.

The formation of optical WGMs in a spherical microcavity occurs as follows. If the refractive index of a nonabsorbing sphere is larger than the refractive index of the material surrounding it, then a beam of light approaching the internal sphere surface at an angle above the critical angle (with respect to the sphere surface normal) will be totally internally reflected at the sphere-air interface [41, 49, 34]. When the circumference of the sphere is larger than at least a few wavelengths of light, the light can undergo multiple reflections off the curved inner surface of the sphere, and produce resonance (constructive interference) when it returns in phase to the starting position. The ray of light inside the sphere stays close to the inner surface because the angle of incidence (with respect to the sphere surface normal) must be large enough for total internal reflection (TIR) to occur. To illustrate this point, an example of a ray path is shown in Figure 2.3. The energy density is highest close to the inner sphere surface, giving the light a ring-like appearance.

In reality, a description of light propagating around the sphere by a series of total internal reflections cannot be entirely explained by geometric optics. According to

this picture, light could neither enter the sphere nor leave it. The light must enter the sphere at an angle beyond the critical angle in order to be trapped inside, which is impossible by simple refraction. The only way for the light to enter the sphere is by diffraction or optical tunneling (frustrated TIR) [34]. The TIR modes are then trapped inside the sphere with a loss of light due only to scattering and absorption in the sphere. The modes are able to radiate due to scattering (otherwise, in a perfect sphere, they would be trapped inside forever). However, even with this loss, the light is nearly totally internally reflected and it takes a long time to escape the sphere [34]. This efficient trapping of light in a spherical microcavity is what makes the extremely high Q factors possible.

In this way, a uniformly solid microsphere can be used as a cavity for trapping light into high Q WGMs. The source of light (eg. fluorescent nanocrystals) could be inside the microsphere or outside the microsphere. As discussed in Section 2.2.1, resonant wavelengths of light are intensified in the microsphere, and corresponding widely separated intense peaks appear in the emission spectrum of the microsphere (i.e. the WGMs).

Quantum Numbers

The resonance structure inside a spherical microcavity is solely dependent on the size, shape, and refractive index of the cavity. The resonant modes can be described in terms of wavelength λ, frequency f, or size parameter x. The size parameter is defined as

$$x = \frac{2\pi a}{\lambda} \tag{2.9}$$

where a is the radius of the sphere.

Each cavity mode has a unique set of quantum numbers, or *order numbers*, that describe the angular dependence of the electric field inside the sphere. Each mode is indexed by three numbers, n, l, m, which are all integers, and correspond to the number of intensity maxima in a given direction. The angular order number (or mode number), n, can be thought of as the approximate number of wavelengths that fit inside the sphere. It gives the number of maxima in the field intensity from polar angle 0^o to 180^o. The radial order number (or order number), l, represents the number of maxima in the field intensity in the radial direction. And lastly, the

azimuthal order number (or magnetic number), m, describes the angular dependence from azimuthal angle 0^o to 360^o. m can be anywhere from $-n$ to n, where positive or negative m is given to waves traveling in opposite directions around the sphere's equator (so that the total number of maxima will be $2|m|$). For perfect spheres, modes differing only in azimuthal number m are degenerate (have the same resonance spectrum). When a particle is not exactly spherical, modes for different m values become nondegenerate, and the frequency shift between them is related to the ellipticity of the sphere [34].

For small size parameters, the first-order modes are the first to appear in the spectrum, and they occur when $n \approx Nx$ where x is the size parameter and N is the refractive index. As the size parameter is increased, the linewidths decrease and the order number, n, increases. The relation $n = Nx$ equates the number of wavelengths inside the sphere to the circumference of the sphere:

$$n_{max}\frac{\lambda}{N} = 2\pi a \tag{2.10}$$

Here the label n_{max} is given since this represents the maximum number of wavelengths that fit inside the sphere (or the maximum value of angular momentum). If n is higher than n_{max}, the energy densities of the modes are mostly outside the sphere, and hence are extremely lossy. From this equation, it can be seen that n_{max} increases with increasing size of sphere, since more wavelengths can fit inside a larger sphere.

Looking at the other extreme, the minimum number of wavelengths that can fit into the sphere and produce resonance corresponds to $n_{min} = x$, so that the broadest modes to appear in the spectra have $n \approx x$. If n is less than n_{min}, the light approaches the internal surface of the sphere at an angle greater than the critical angle and therefore is not confined within the sphere by total internal reflection [34] (see Figure 2.4). So we have:

$$n_{min} = \frac{2\pi a}{\lambda} \tag{2.11}$$

In summary, from Equations 2.10 and 2.11, we have [58] :

$$x < n < Nx \tag{2.12}$$

Here the highest n values correspond to the modes with the greatest confinement and hence the highest possible Q values (in this case, m is close to n and l=1). The

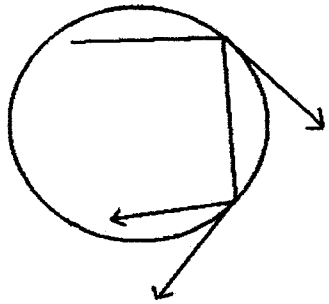

Figure 2.4: When $n < n_{min}$, the light is no longer confined in the sphere by total internal reflection. At each reflection point, some light is reflected inside, and some escapes outside the sphere.

lowest n values correspond to the lowest possible Q values that can occur when the sphere is still resonant with light.

TE and TM Modes

When dealing with an electromagnetic wave crossing the boundary between a sphere and its surrounding medium, the boundary conditions depend on the polarization of the field. This leads to two types of resonances that can exist in the sphere: transverse electric (TE) – with the electric field perpendicular to the plane of incidence, and transverse magnetic (TM) – with the electric field parallel to the plane of incidence [45]. The plane of incidence is the plane containing the incident and reflected rays (i.e. the plane of the paper, as in Figure 2.5). Due to their polarization direction, the TM modes extend slightly outside the sphere compared to the TE modes [77]. TE modes are hence associated with higher Q values and more efficient confinement of light than TM modes [77].

In the emission spectrum, it is possible for TE and TM modes to appear as one peak, when they are very closely spaced and broad [34]. This effect will lessen as size parameter is increased (i.e. as wavelength is decreased, since $x = 2\pi a/\lambda$). However, in general the TE and TM modes occur at different wavelengths and appear as separate peaks. The shift in wavelength between TE and TM modes with the same order numbers n, l, and m is due to the Fresnel phase-shifts upon reflection [55].

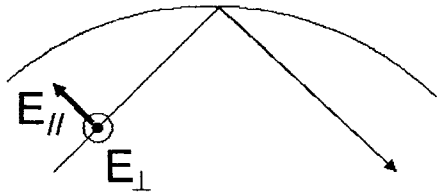

Figure 2.5: The two polarizations of light in a sphere: with the electric field perpendicular to the plane of incidence ($E_\perp$, corresponding to TE modes) or with the electric field parallel to the plane of incidence ($E_{//}$, corresponding to TM modes). The plane of incidence is the plane of the paper.

This shift, in terms of frequency, is given by [55, 72] :

$$\Delta f_{TE-TM} = \frac{(N^2-1)^{1/2}\Delta f_{FSR}}{N} \tag{2.13}$$

where N is the refractive index of the sphere as usual, and Δf_{FSR} is the free spectral range in terms of frequency. A theoretical formula for calculating Δf_{FSR} will be given below in the "Free Spectral Range" subsection.

Resonance Locations

It is possible to calculate with high accuracy the theoretical positions of low order (low l) modes of any given polarization and quantum number by using high-order asymptotic expansion formulas. Since WGMs correspond to low l values, this is directly useful in the present work. Many approximate analytical formulas for the resonance locations have been calculated according to Mie theory. One of the most accurate of these was derived by Schiller in 1993 [71]. He showed that the resonance locations (in terms of size parameter x) are

$$x_n^l = \frac{\nu}{M} - \frac{\zeta_l}{M}\left(\frac{\nu}{2}\right)^{1/3} + \sum_{k=0}^{k_{max}} \frac{d_k(M,\zeta_l)}{\nu^{k/3}(M^2-1)^{(k+1)/2}} \tag{2.14}$$

where $\nu = n + 1/2$, $M = N_s/N_a$ is the relative index of refraction of the sphere (s) to the surrounding medium (a), ζ_l is the lth root of the Airy function which can be found in standard mathematical tables (see for example [54]), and $d_k(M,\zeta_l)$ is a coefficient that depends on M and ζ_l. The limit k_{max} refers to the highest k value taken for the summation. The higher k_{max} is, the more accurate the approximation is. The coefficients $d_k(M,\zeta_l)$ are not well known for high k and require much

calculation to find. In Schiller's paper [71], the coefficients for $k = 0$ to $k_{max} = 8$ are given (thereby offering higher accuracy than in previous calculations which had used $k_{max} = 2$ [72, 54]). As an example, the first four coefficients are:

(2.15a) $$d_0 = -p$$

(2.15b) $$d_1 = \frac{2^{1/3}3(M^2-1)\zeta_l^2}{20M}$$

(2.15c) $$d_2 = \frac{-2^{2/3}M^2p(-3+2p^2)\zeta_l}{6}$$

(2.15d) $$d_3 = \frac{350M^4(1-p)p(-1+p+p^2)+(M^2-1)^2(10+\zeta_l^3)}{700M}$$

where $p = 1$ for TE modes and $p = 1/M^2$ for TM modes. Here the resonances are given in terms of size parameter x. If the size of the sphere is known, the resonant wavelengths can also be calculated by Equation 2.14 using $\lambda = 2\pi a/x$.

Free Spectral Range

The free spectral range in a spherical microcavity can now be defined more properly as the spacing between neighbouring whispering gallery modes of the same polarization with the same radial (l) and azimuthal (m) order numbers, but a difference of one unit of angular order number (n) (i.e. two successive modes of the same transverse mode structure). There are two approximations for free spectral range that are commonly quoted by various authors. The first has been quoted with respect to fluorescent spheres [58, 34]:

(2.16) $$\Delta x_{FSR} \approx \frac{\tan^{-1}[(N^2-1)^{1/2}]}{(N^2-1)^{1/2}}$$

where N is the refractive index of the sphere.

The second equation is more often used for Mie scattering. It is derived under the assumption that the mode number n is approximately equal to the number of wavelengths that fit inside the sphere, and that the mode's electric field at the surface of the sphere is approximately zero. In terms of frequency, the free spectral range is [55, 72]:

(2.17) $$\Delta f_{FSR} \approx \frac{c}{2\pi Na}$$

where f is the frequency, c is the speed of light, N is the refractive index, and a is the sphere radius.

Rate Enhancement η

The cavity rate enhancement, η, is the magnitude of the enhancement of the probability for spontaneous emission at resonance as compared to free space. It is given in [58] by

$$\eta = \frac{3\lambda^3 QD}{4\pi^2 V_m} \tag{2.18}$$

where D is the degeneracy of the mode, Q is the quality factor, and V_m is the mode volume. Comparing this to Equation 2.6, we see that the rate enhancement η is just another form of the Purcell factor P. The enhancement can be approximated by

$$\eta \approx \frac{9\sqrt{2}N^2 Q}{x^{3/2}} \tag{2.19}$$

where N is the refractive index, Q is the quality factor, and x is the size parameter (see [58] for the derivation of Equation 2.19 from Equation 2.18). This approximation holds under the following assumptions: (1) Q is low, (2) Q is much less than Q_{ab}, and (3) $n \approx x$. Q_{ab} is the absorption factor and is given by $Q_{ab} = 2\pi N/\alpha\lambda$ [58]. Here α is known as the absorption coefficient, and it is a measure of the purity of the sphere. If the sphere is perfectly pure (with no defects), then $\alpha = 0$.

Note that the rate enhancement of spontaneous emission also depends on the location of the light emitter inside the spherical cavity. Both theory [18, 17, 15] and experiment [88] have shown that when the emitter is near the surface, the enhancement is great (over 1000 times that of the free space value), but for light emitters in the central portion of the sphere there is no enhancement.

The Q factor

Although the Q factors of spherical microcavities can be extremely high, there are limiting factors, such as surface imperfections, which can seriously lower Q. The overall Q-factor can be broken down into all its contributing mechanisms as follows [77]:

$$\frac{1}{Q} = \frac{1}{Q_{mat}} + \frac{1}{Q_{WGM}} + \frac{1}{Q_{ss}} + \frac{1}{Q_{contam}} + \frac{1}{Q_{coupling}} \tag{2.20}$$

Each of the terms on the right hand side of Equation 2.20 represents some form of loss from the cavity. Q_{mat} is due to resonator material loss, Q_{WGM} is due to the curved dielectric cavity, Q_{ss} is due to scattering off of surface imperfections, Q_{contam} is due to contamination on the surface or inside the cavity, and $Q_{coupling}$ is due to input/output coupling.

Gorodetsky et al. performed a study on the ultimate Q of optical microsphere resonators [30]. They found that the limit for microsphere Q at 633 nm is 0.9×10^{10}, but that in regular laboratory conditions Q will worsen within 1 h, due to water vapours and dust accumulating on the microsphere surface. They propose that in order to preserve high Q, the microspheres must be made and kept in evacuated dry-gas-filled chambers or be treated chemically to prevent surface hydration. In the present case no special care was taken with respect to the storage of the microspheres since the dominant loss mechanisms should be due to the film itself rather than contamination on the surface of the film.

2.3 Experimental Background

With the basic theory of nanocrystals and spherical microcavities now presented, this section is devoted to how nanocrystals and microspheres have been used in combination by other researchers. The work discussed here is what leads up to the experimental design used in this thesis research (which follows in Chapter 3).

Glass or polymer microspheres are amongst the common types of spherical microcavities that are known to produce high Q WGMs (as an example, another type would be a liquid droplet). High Q modes and lasing have often been observed when the microsphere is coupled with laser beam light. Of particular interest, even single mode lasing was achieved by Cai et al. [10] when they tuned the pump laser's wavelength to the fundamental WGM resonance of the sphere.

The possibility of developing a light source from microspheres coupled to the luminescence of QDs has also been widely studied both theoretically and experimentally. For example, Pelton and Yamamoto have proposed a design for a semiconductor micro-laser which couples the light emitted from a single InAs/GaAs QD into the WGMs of a glass microsphere [66]. This would be achieved by bringing a glass microsphere attached to a fiber stem very close to the surface of a GaAs matrix

with a single InAs QD embedded inside. The calculated threshold current for this laser is several orders of magnitude lower than for other semiconductor lasers.

Experimental researchers have also investigated microsphere/nanocrystal devices. Sometimes the QDs in these structures are formed inside the sphere, but it was noted by Artemyev et al. [7] that since the electromagnetic field is highest at the surface of the sphere, it would be best to attach the QDs to the surface of the microsphere or embed them in a thin shell of a hollow microsphere. Many different methods of attaching the nanocrystal to the microsphere have been tried by different authors. Jia et al have reported on $CDSe_xS_{1-x}$ QDs embedded in glass microspheres ($\sim$40 μm diameter) with observed resonance modes of $Q = 1790$ [41]. The microspheres were formed by a heating process of glass containing CdO, CdS, and elemental sulfur or selenium. The spheres were annealed for several hours to form $CDSe_xS_{1-x}$ nanocrystals inside by precipitation. Artemyev et al. have used glass microspheres ($3 - 10$ μm diameter) with ZnS-coated CdSe nanocrystals attached to the surface in a thin shell to achieve Q factors greater than 10^4 [7]. The nanocrystals were chemically bonded to the surface of the microsphere via a process known as mercaptosilanes. Klimov and Bawendi coated polystyrene microspheres (10 μm diameter) with a thin film of CdSe nanocrystals (<100 nm thick) and achieved lasing from these structures [47]. The number of lasing modes increased with excitation power. As well, a recent report by Snee et al. showed lasing from silica and polystyrene microspheres coated with CdSe/CdZnS nanocrystals [76]. The microspheres were coated uniformly to preserve sphere structure by mixing them with a nanocrystal/titania solution.

Reports on high Q WGMs and lasing from microsphere/nanocrystal structures usually have used direct gap semiconductor nanocrystals. There have been studies in which silicon nanocrystals were implanted into microspheres, but strong WGMs were not found in the spheres. For example, in a work by Ryan et al., silicon nanocrystals were embedded into silica microspheres via ion implantation [70]. This study hinted that the light was being coupled into WGMs, however the modes were very weak. The process of ion implantation caused the spheres to be severely deformed, making them more muffin-shaped than spherical (see Figure 2.6), and hence there were no resonant modes inside the cavity.

In other work, silicon nanocrystals were embedded via ion implantation into silica

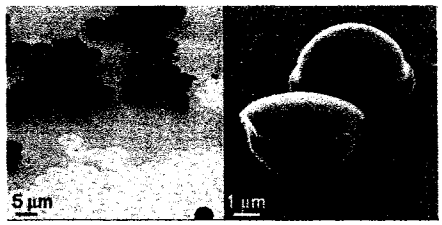

Figure 2.6: 5 μm diameter silica microspheres that have been implanted with Si nanocrystals by ion implantation. Figure reproduced from [70].

microspheres or nanospheres for the purpose of patterning them into 2D arrays or 3D artificial opals [82, 2, 96]. Again, little to no WGMs were observed, but these works showed successful patterning of the microspheres. Such patterning of the spheres offers further control over the emission properties, making them attractive for potential device applications. As an example, a periodic structure of materials with alternating dielectric constants is known as a photonic crystal [42]. Scattering at the interfaces between the different dielectric constants causes photons of certain frequencies to be forbidden to propagate through the crystal (much like the case of an energy band gap for electrons in semiconductor materials). Depending on the geometry of the crystal, certain frequencies can be allowed in one direction while others are forbidden, thereby offering control over the direction of emission from the crystal. In fact, the patterning of luminescent nanocrystals to make the emission more directional has been studied using various techniques such as lithography [61, 37]. Attaching the nanocrystals to microsphere arrays is just one of these methods.

Many researchers have studied the theory involved with luminescent microsphere arrays, but not very many experimental studies have been done since arrays with large areas are difficult to make. Researchers are experimenting with methods to make arrays, such as lithography and self-organization methods [95, 84, 82]. For example, Yamasaki and Tsutsui reported a method which produces two dimensional arrays of silica microspheres as big as 3 cm^2 in area [95]. Their technique involves a reservoir and a tapered cell filled with a suspension, placed in a specific set-up such that an array is formed by self-organization as the suspension drys. The hexagonal arrays were found to be uniform (with some imperfections due to variations in sphere size) and they withstood various chemical and thermal treatments.

Chapter 3

Experiment

3.1 Experiment Goals

There were two main experimental goals to this thesis research. The first was to develop a new structure using silicon nanocrystals and silica microspheres that would not deform the spheres and hence could be used to trap light efficiently into the WGMs. The second goal was to study the optical properties of this structure and experiment with different parameters to control the PL spectrum. With these goals in mind, arrays of silica microspheres were arranged onto a substrate and coated with a thin layer of silicon nanocrystals on top (Figure 3.1). The idea here is that by putting the nanocrystals on the outside of the sphere, ion implantation could be avoided so that deformation of the sphere would not take place as in previous work [70]. Instead electron-beam evaporation was used in combination with annealing to "grow" the nanocrystals on top of the sphere. The luminescence from the nanocrystal could then enter the sphere through the upper hemisphere and ideally be trapped into the WGMs. Aside from avoiding ion implantation as a preparation method, placing the nanocrystals on top of the spheres is advantageous for another reason. As mentioned in Chapter 2, enhancement factors are greatest for emitters near the surface of the sphere as opposed to the central portion. Also, when WGMs are trapped inside a sphere, the electromagnetic field is highest close to the surface, so that for maximum confinement of light the ideal place for the emitter is either attached to the surface of a solid sphere, or embedded in a thin shell around the edges of the sphere [7].

Figure 3.1: Experimental Samples: an array of silica microspheres on a substrate with a layer of Si nanocrystals on top. Drawing is not to scale.

The spheres were aligned in monolayer arrays to show that, in principle, such structures could be used for photonics applications in which the emission should be directional. Tuning of the luminescence wavelength was not attempted, however, various sphere sizes and thicknesses of nanocrystal film were used in order to provide some controllability on the PL spectrum.

The experimental portion of this research involved preparing the samples (as will be discussed in Section 3.2) and collecting photoluminescence measurements and images of these samples (as in Section 3.3). The goals of these experiments were to identify and understand the differences in PL spectra for different sizes of microspheres, different thicknesses of the Si nanocrystal film, a single sphere vs an array of spheres, and different locations within a single sphere (i.e. center vs the edges).

3.2 Sample Preparation

Preparing luminescent microsphere arrays was a three-step process that took about four days in total to complete. The three main steps were: (1) Drop-coating the spheres onto a substrate to form an ordered array (Section 3.2.2), (2) adding a thin film of SiO_x on top of the array of spheres by electron-beam vapor deposition (Section 3.2.3), and (3) annealing the samples to form nanocrystals inside the film (Section 3.2.4).

3.2.1 Microspheres

The standard materials for making microspheres used in research are silica and polymer (ex. polystyrene or polyMMA). Since the refractive index of solid materials is greater than that of air ($N = 1$), which is usually the surrounding medium, then WGMs can be achieved. Some groups use plastic microspheres (polymer $N = 1.5$), while most choose silica or glass microspheres because of their better optical stability.

Polymer microspheres often degrade in optical experiments due to photosensitive surface reactions, while silica spheres do not [41].

Microspheres can be prepared using a chemical method [5], but the most common way involves heating a material and allowing surface tension to form the sphere [41, 49, 53, 66]. For this thesis research, microspheres were ordered from commercial suppliers. They came in a small bottle dispersed in a solution of deionized water. Four sizes of spheres were ordered from Bangs Laboratories, having nominal diameters of 4.99 μm, 3.47 μm, 2.34 μm, and 0.80 μm, with a quoted standard deviation of 10 %. Another bottle of 20 μm diameter spheres was ordered from Kisker. These spheres had a very high standard deviation on the size distribution (although it was not given by the supplier, the standard deviation was later estimated to be around 50 % by imaging of the spheres). The spheres were made from pure silica (glass), which is a uniform, amorphous (noncrystalline) solid material. According to both suppliers (Bangs Labs and Kisker), all the spheres had a refractive index of 1.37, which is somewhat lower than commercial fused silica.

3.2.2 Drop-Coating Spheres onto a Substrate

In order to produce long-range two-dimensional arrays, the spheres were deposited onto substrates using the drop-coating technique outlined in reference [84]. In this method, spheres in solution are dropped onto an angled substrate that has been treated by potassium hydroxide (KOH). As the spheres dry and make their way down the angled substrate, they naturally form hexagonal close-packed arrays.

Fused silica substrates ($\sim$6.5 cm^2 in area and $\sim$1 mm thick) were left overnight in a covered flask of KOH to increase their hydrophylicity. In this treatment, a chemistry change in the substrate takes place which causes a drop of water on the surface of the substrate to be "flat" as opposed to forming the usual convex "bubble" that it would form on glass or plastic. After the KOH treatment, the substrates were cleaned to remove the excess KOH. The cleaning process consisted of putting the substrates into clean distilled water and sonicating for a few minutes. This was repeated 2 - 3 times using a new flask of water each time. The bottle of spheres was also sonicated briefly ($\sim$30s) to shake up the spheres, which were often stuck in a clump at the bottom of the bottle. Once the sonication was complete, the substrates were taken out of the distilled water and mounted at an angle of $\sim 10^o$ to

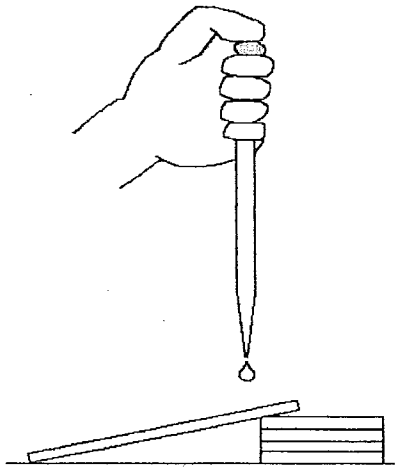

Figure 3.2: Spheres in solution are dropped onto an angled substrate propped up by a few microscope slides (drawing not to scale – the size of the substrate and slides has been exaggerated for clarity).

the horizontal by resting their edges on a stack of 2 - 4 microscope slides. While the substrates were still wet, the spheres (in water) were deposited onto the substrate using a micropipette. One small drop was deposited near the top central portion of each substrate (see Figure 3.2). Next, the substrates were covered by a bell jar and left to dry for 2 - 3 days. The drying took place at room temperature in a relatively vibration-free area of the lab. To ensure slow drying, the atmosphere was kept moist by including an open flask of water inside the bell jar. A moist atmosphere is important in order to create well ordered arrays [84].

3.2.3 Electron-Beam Evaporation

After drying, the microsphere arrays were coated with a thin film of nanocrystals. The experimental basis for the nanocrystal synthesis method was developed by Glover and Meldrum [28], which itself was based on earlier work by Kahler and Hofmeister [44]. In this method, thin film physical vapor deposition is used to form a thin film of silicon rich oxide (SiO_x, where $1 < x < 2$). The film can be formed by co-evaporating such materials as silicon (Si), silicon monoxide (SiO), and silica (SiO_2). Alternatively, a single material such as SiO can be evaporated in the

presence of oxygen to make SiO_x with $x > 1$. The pressure of the oxygen within the evaporation chamber can then be used to control the film composition. Both methods were used for this research: single source evaporation and co-evaporation of two sources.

Method 1 (Single Source Evaporation)

In this method, a single source material was used as the evaporant. A schematic of the evaporation chamber is shown in Figure 3.3. The substrates, pre-coated with arrays of spheres, were mounted at the top of the chamber directly above the source evaporant. In order to ensure stable evaporation rates, a molybdenum crucible with a tungsten lid was used. The electron beam was directed at the lid and heated the crucible more-or-less uniformly. The evaporated material escaped into the chamber through a small hole in the lid. This system controlled the problem of spitting that is a typical difficulty with molten silicon monoxide. The evaporation rate was controlled via the emission current of the electron gun. The amount of evaporant reaching the substrates was measured by a crystal thickness monitor mounted at the same height. Once the desired film thickness was reached, the substrates were blocked from further deposition by a shutter just below them. There may have been some consistent error in the crystal monitor measurement, but this would not affect the conclusions of the present study (since exact film thicknesses were not important).

Silicon monoxide (SiO) was used as the evaporant and the deposition was performed with a continuous flow of oxygen in the evaporation chamber in order to produce a film composition of SiO_x. The oxygen pressure in the chamber was always set at 1×10^{-5} Torr just before the evaporation, but during the evaporation the oxygen pressure was reduced due to gettering (oxygen reacting with the evaporant and sticking to the walls of the chamber). This method usually results in a film composition of approximately $SiO_{1.2}$ when the evaporation pressure is $\sim4\times10^{-6}$ Torr [28]. Although this composition was aimed for by setting the pre-evaporation pressure to 1×10^{-5} Torr, during deposition the pressure could not be adjusted. In each deposition the pressure was different, ranging from $\sim5\times10^{-6}$ Torr to 1×10^{-5} Torr (see Table 3.1 and 3.2). In most cases, the pressure was between $\sim2\times10^{-6}$ Torr to 6×10^{-6} Torr. However, in one deposition (of 20 nm film) the pres-

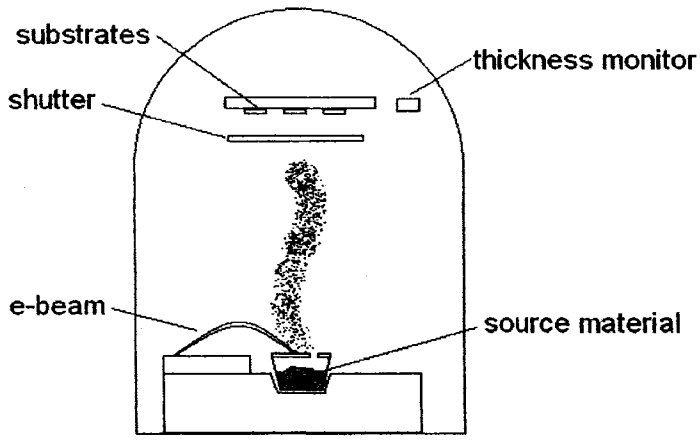

Figure 3.3: The electron-beam evaporation system.

sure was $\sim 1 \times 10^{-5}$ Torr which is quite a bit higher than the others, meaning that the film composition had a higher concentration of oxygen. However, since these films showed characteristic silicon nanocrystal PL, these samples were included for WGM analysis.

Method 2 (Co-evaporation of Two Sources)

Method 2 is similar to Method 1, except that instead of bleeding oxygen into the chamber, an additional source (SiO_2) was used in combination with the SiO to produce a composition of SiO_x. This has the advantage of obtaining higher x values. With Method 1 the upper limit is $x = 1.2$. In this work, Method 2 was used to produce films of $x = 1.4$, which has been shown to be a composition that produces strong PL.

In this method, one source (SiO_2) was placed in the crucible and was heated via the e-beam as described above. The other source (SiO) was placed in a "boat" near the middle of the chamber that was heated thermally. The two sources were heated (and hence evaporated) simultaneously. Two thickness monitors were mounted at the height of the substrates, one to measure the thickness of material contributed by

each source. The path of evaporation for each source was shielded in order to reach the appropriate monitor only. By careful control of the evaporation rates of both sources, and timing of the deposition, it was possible to control the composition of the film. For example, in one deposition the SiO was evaporated at a rate of 3 Å/s while the SiO_2 was evaporated at 2 Å/s. The total deposition time was two minutes, resulting in a 100 nm film of $SiO_{1.4}$.

3.2.4 Annealing

After the SiO_x films were deposited onto the arrays of spheres, the samples were then ready for annealing. When the film is annealed, the SiO_x phase separates to form an Si + SiO_2 mixture. There has been much debate concerning the diffusion, nucleation, and growth processes at work and many authors have investigated the effect of annealing temperature and annealing time on the particle size and size distribution. For a given SiO_x composition, a higher annealing temperature results in larger silicon particles. If the temperature is too high, this could cause large particles or semi-continuous layers of silicon to form [59]. The exact effect of the annealing time is not as clear. Some researchers have observed PL redshifts by increasing the annealing time and have hence concluded that nanocrystal size is increased with longer anneals (eg. see [74]). But in another study, López et al. [56] showed that nanocrystal size was unaffected by different annealing times (1 minute or 16 hours made no difference), but PL intensity was affected. The PL intensity increased with annealing time up to 4 hours and then saturated. The annealing atmosphere also plays a role: several investigations have shown that the presence of hydrogen in the annealing atmosphere is crucial for obtaining reasonably intense luminescence [63, 90, 27, 35]. This is thought to be due to the hydrogen passivation of silicon dangling bonds at the nanocrystal-matrix interface (dangling bonds - i.e., P_b centers - are well known nonradiative traps in silicon).

The samples in this work were annealed for 1 h at 1000 °C in flowing 96% N_2 + 4% H_2 gas at a pressure slightly above 1 atm. The annealing temperature was chosen on the basis of previous experiments by Glover [27], who showed that SiO_x films annealed for 1 h at 1000 °C gave more intense luminescence (an order of magnitude greater) than those annealed for 1 h at 600 °C, 800 °C, or 1200 °C. The annealing gas was chosen in order to passivate nonradiative traps and enhance the

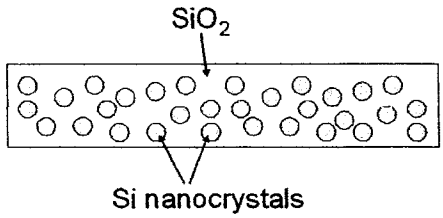

Figure 3.4: An SiO_x film annealed to form Si nanocrystals embedded within an SiO_2 film.

luminescence. Previous research [27] has shown that $SiO_{1.2}$ films annealed under these conditions (1 h at 1000 °C in N_2 + H_2) result in an SiO_2 film embedded with randomly oriented Si nanocrystals with an average diameter of approximately 3 nm and an average interparticle spacing of approximately 3 nm (Figure 3.4).

3.2.5 Sample Lists

Using the above outlined method of drop-coating, e-beam evaporation, and annealing, several samples were prepared. $SiO_{1.2}$ films 20 nm, 50 nm, and 100 nm thick were deposited onto each of the four Bangs laboratories sphere sizes using evaporation Method 1. The 20 μm spheres that were ordered from Kisker were examined much later in the research in order to test the Q factor of relatively large spheres. By this time, the $SiO_{1.4}$ composition was found to produce more intense luminescence as compared to the $SiO_{1.2}$ composition, so the 20 μm spheres were deposited with $SiO_{1.4}$ films using evaporation Method 2. For a list of all main samples prepared, see Table 3.1. Samples were named according to their sphere diameter and film thickness.

In addition to the main experiments, a number of preliminary samples were prepared to test such factors as film composition. These included a set of "blank" samples, a set of "three stages" samples, and a set of "$SiO_{1.4}$" samples. The "blank" samples were prepared without any film on top of the spheres to see if any luminescence originated from the spheres themselves. The "three stages" samples were prepared to compare the sample structure in the three main stages of preparation: I (drop-coated), II (drop-coated and deposited on) and III (drop-coated, deposited on, and annealed). The "$SiO_{1.4}$" samples were deposited with $SiO_{1.4}$ using evaporation Method 2 to compare to those made with Method 1 and test film composition

List of Main Samples				
Sample	Sphere Diameter (μm)	Film Thickness (nm)	Targeted Film Composition	Deposition Pressure (Torr)
0.8μm100nm	0.80	100	$SiO_{1.2}$	2×10^{-6}
2.34μm100nm	2.34	100	$SiO_{1.2}$	2×10^{-6}
3.5μm100nm	3.47	100	$SiO_{1.2}$	2×10^{-6}
5μm100nm	4.99	100	$SiO_{1.2}$	2×10^{-6}
0.8μm50nm	0.80	50	$SiO_{1.2}$	6×10^{-6}
2.34μm50nm	2.34	50	$SiO_{1.2}$	6×10^{-6}
3.5μm50nm	3.47	50	$SiO_{1.2}$	6×10^{-6}
5μm50nm	4.99	50	$SiO_{1.2}$	6×10^{-6}
0.8μm20nm	0.80	20	$SiO_{1.2}$	1×10^{-5}
2.34μm20nm	2.34	20	$SiO_{1.2}$	1×10^{-5}
3.5μm20nm	3.47	20	$SiO_{1.2}$	1×10^{-5}
5μm20nm	4.99	20	$SiO_{1.2}$	1×10^{-5}
20μm100nm	20	100	$SiO_{1.4}$	2×10^{-6}
20μm50nm	20	50	$SiO_{1.4}$	2×10^{-6}
20μm20nm	20	20	$SiO_{1.4}$	3×10^{-6}
20μm5nm	20	5	$SiO_{1.4}$	3×10^{-6}

Table 3.1: List of samples showing sphere diameter (according to the supplier), film thickness (according to the crystal monitor), targeted film composition (according to whether deposition Method 1 ($SiO_{1.2}$) or 2 ($SiO_{1.4}$) was used, and average pressure during the deposition of the film (according to the pressure monitor of the E-beam system). All samples were annealed for 1 h at 1000 °C).

List of Preliminary Samples				
Sample	Sphere Diameter (μm)	Film Thickness (nm)	Targeted Film Composition	Deposition Pressure (Torr)
0.8μmblank	0.80	-	-	-
2.34μmblank	2.34	-	-	-
3.5μmblank	3.47	-	-	-
5μmblank	4.99	-	-	-
20μmblank	20	-	-	-
5μm50nm(I)*	4.99	-	-	-
5μm50nm(II)*	4.99	50	$SiO_{1.2}$	1×10^{-5}
5μm50nm(III)	4.99	50	$SiO_{1.2}$	1×10^{-5}
0.8μm50nm(1.4)	0.80	50	$SiO_{1.4}$	3×10^{-6}
2.34μm50nm(1.4)	2.34	50	$SiO_{1.4}$	3×10^{-6}
3.5μm50nm(1.4)	3.47	50	$SiO_{1.4}$	3×10^{-6}
5μm50nm(1.4)	4.99	50	$SiO_{1.4}$	3×10^{-6}

Table 3.2: List of preliminary samples showing sphere diameter (according to the supplier), film thickness (according to the crystal monitor), targeted film composition (according to whether deposition Method 1 ($SiO_{1.2}$) or 2 ($SiO_{1.4}$) was used, and average pressure during the deposition of the film (according to the pressure monitor of the E-beam system). All samples were annealed for 1 h at 1000 °C except * which were not annealed.

effects. A list of all preliminary samples is given in Table 3.2.

3.3 Photoluminescence Spectroscopy and Imaging

The samples consisted of areas of arrays of spheres near the center, and more dispersed spheres near the edges of the deposited area. Therefore we were able to collect PL from not only an ensemble of spheres, but single spheres as well. The photoluminescence spectroscopy method used was different for the case of ensembles and single spheres and will be given in Sections 3.3.1 and 3.3.2, respectively. Fluorescence, reflection, and transmission images of single spheres and arrays were also taken for all samples, as discussed in Sections 3.3.3 and 3.3.4.

3.3.1 Ensemble Spectroscopy

The set-up used for collecting photoluminescence spectra of arrays of spheres ("ensemble spectra") is shown in Figure 3.5. The 325 nm line of a HeCd laser with a continuous wave (CW) power of ~20 mW and a diameter of ~1 mm^2 was used as the excitation source. Using a mirror, the beam was directed towards the sample at an area of arrays (this area was visible by eye, as will be discussed in Chapter 4). The PL was collected by an optical fiber and brought through a long-pass filter to a 2048-pixel linear CCD spectrometer. The filter was used to block reflected laser light from being collected by the spectrometer. The spectrometer was attached to a computer, where spectra were collected using the program OOIbase. The spectral response of the spectrometer was calibrated using a standard blackbody radiator.

3.3.2 Single-Sphere Spectroscopy

Single-sphere spectra were taken on a home-built photoluminescence microscopy setup. Isolated spheres were first lined up under an optical microscope. The 442 nm line of a HeCd laser was then directed into the microscope and focused through the objective lens and onto the sample to excite the PL. The PL was collected from the same objective and then directed through a 550 nm long-pass interference filter to remove reflected laser light, and onto an imaging spectrograph interfaced to two CCD cameras (one for imaging and the other for spectroscopy). The spectral response of the system was corrected using the same blackbody radiator as for the

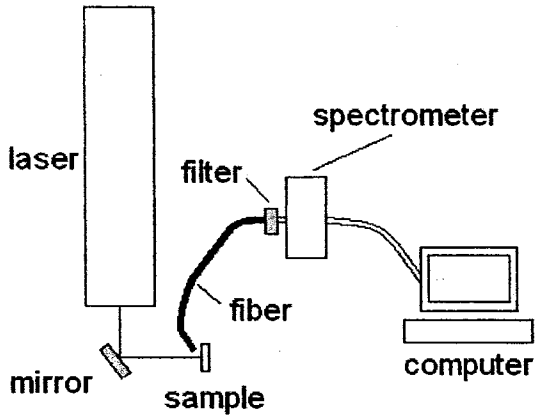

Figure 3.5: The set-up used for collecting ensemble photoluminescence spectra.

ensemble PL measurements. The wavelength scale of the resulting spectra was determined by calibrating with an HgAr lamp. Spectra were collected on the computer using the programs SBIG Spectrograph and CCDops. An image of the sphere was displayed on the computer along with the entrance slit of the spectrometer. The slit could be lined up with any desired portion of the sphere. Also, the emission collected through the spectrometer slit could be cropped in order to compare light emission from different areas of the sphere (i.e. the center vs. the edges).

Using this set-up it was also possible to analyze the PL of the sphere from different angles. Usually, the substrate was face up in the microscope so that the spheres were excited from the top and the PL was collected from the same angle. By cleaving the substrate and propping it on its side, it was possible to obtain images and spectra at a 90^o angle from the substrate surface normal (if the contact point of the sphere with the substrate is the "bottom' of the sphere, then this set-up was the "side view"). This experiment was difficult to do however, because there were very few spheres suitably near the edges of the substrate.

3.3.3 Optical Microscope Imaging

Images were taken through the microscope using a specialized fluorescence camera (Roper Coolsnap E5) and the computer programs WinView and RSImage. The setup allowed images to be taken in three modes: reflection (sample illuminated from

above by a white light), transmission (sample illuminated from below by a white light), and fluorescence (sample excited by a laser, as in Section 3.3.2). Although the camera cannot perform spectroscopic functions, the image quality is superior to the performance of the small CCD used for imaging the slit (see Section 3.3.2). The magnification of the microscope/camera system was calibrated using a standard lithographic array of features with a known size.

3.3.4 SEM

The microstructure of the samples was investigated by a scanning electron microscope (SEM) in the secondary electron imaging mode with a beam energy of 5 kV. The samples had to be coated with a gold film of approximately 150 Å to reduce charging effects, so SEM was the "end of the road" for all samples that were examined. Because of this, samples were always snapped in half before taking to the SEM so that part of the sample could be saved in case it was needed later. The SEM images were taken by George Braybrook (Department of Earth and Atmospheric Sciences) while the author of this thesis was present to guide the selection of images.

Chapter 4

Results and Discussion

In this Chapter the results of the experiments are presented.[1] For convenience, the 4.99 μm diameter spheres will be referred to as "5 μm spheres", the 3.47 μm diameter spheres as "3.5 μm spheres", the 2.34 μm diameter spheres as "2.3 μm spheres", and the 0.80 μm diameter spheres as "0.8 μm spheres". As mentioned previously, the 20 μm spheres were obtained later in the research than the other four sizes (and from a different company) to test Q factors of relatively large spheres. Because of this, the 20 μm spheres will be treated separately in Section 4.2.4.

4.1 Structure of Samples: SEM Results

4.1.1 Sphere Structure

In general, the microspheres maintained their spherical shape throughout the sample fabrication process. A set of three samples was made to examine the structure of the samples in different stages of development: I – after drop-coating the spheres onto the substrate (Figure 4.1 (a) and (b)); II – after depositing a nanocrystal film on top of the drop-coated spheres (Figure 4.1 (c) and (d)); and III – after annealing the coated spheres (Figure 4.1 (e) and (f)).

As shown in Figure 4.1 (and through the examination of many other such images), the deposition and annealing steps did not deform the spheres. There were no consistent differences in the aspect ratio of the spheres before and after anneal-

[1] A version of this chapter will be submitted for publication in the Journal of Luminescence, April 2006 [8].

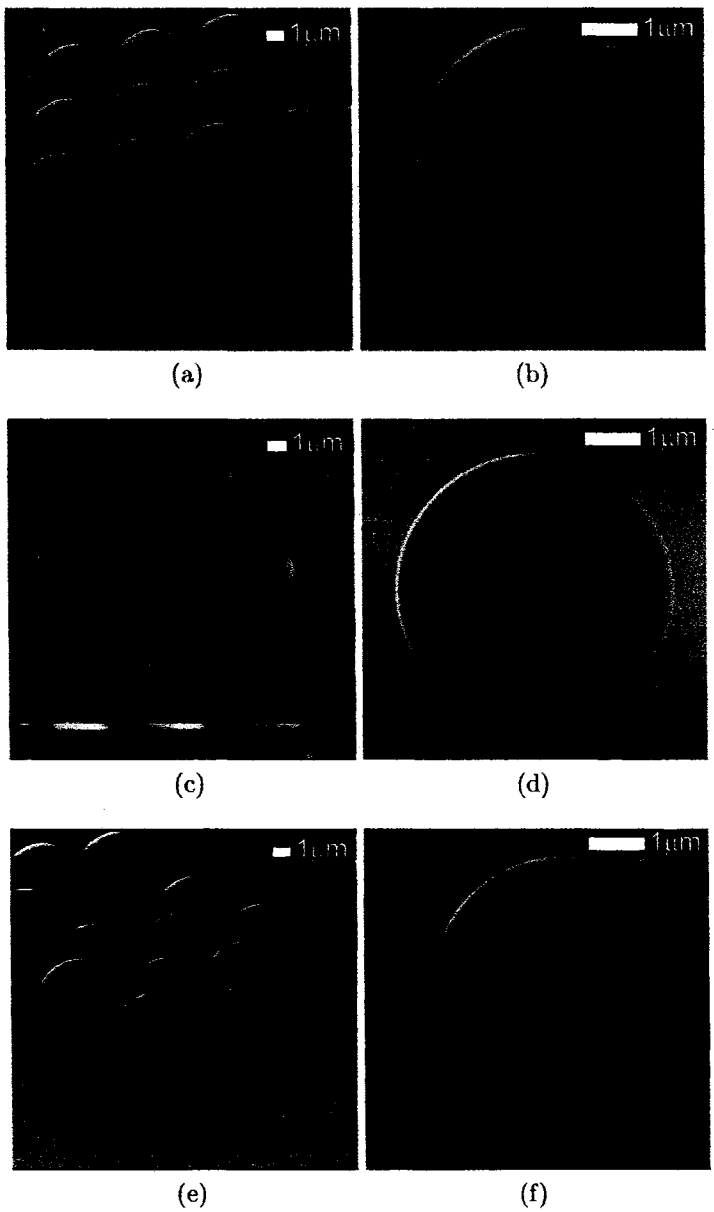

Figure 4.1: SEM images of samples in the three stages of development (all are 5 μm spheres with 20 nm film): (a), (b) after dropping the spheres on the substrate; (c), (d) after depositing the nanocrystal film on top; (e), (f) after annealing. Note the defects in (a) (front row, left) and (c), and the irregular spots (possibly dust or contamination) in (b) and (f). The horizontal white lines in some images are due to charging effects in the microscope. 39

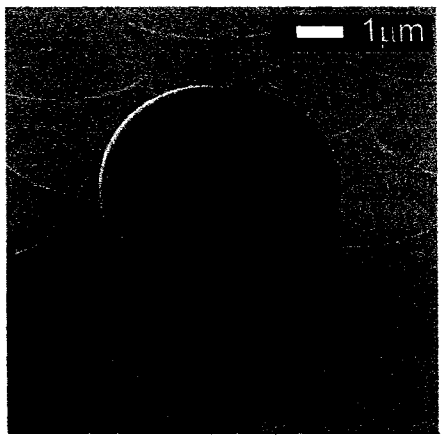

Figure 4.2: SEM image of a "defect" of two or three spheres fused together. This image comes from a sample consisting of 5 μm spheres with 20 nm film.

ing. The only microstructural differences that could be observed between the three stages was the appearance of the film on top of the spheres after deposition. The thin deposited film was visible on the spheres and the substrate. The SiO_x film appeared as a slightly granular structure on the upper section of the spheres, and was clearly evident via a shadowing effect on the substrate (Figure 4.1 (d), (e), and (f)).

Although in general the spheres were not deformed during deposition and annealing, some occasional defects were observed. These were of the form of extra material added onto a sphere (as in Figure 4.1 (c)) or two or three spheres that seemed to have fused together (as in Figure 4.2). Many such defects were observed in the images of the unprocessed spheres (ex. Figure 4.1 (a) and (c)), implying that the sample fabrication did not cause the deformation. The defects may have been caused by the sonication of spheres before drop-coating, but it seems most likely that they were formed in the manufacturing process.

The addition of the nanocrystal film on top of the spheres naturally caused a slight alteration of the shape and texture of the spheres. Looking more closely at the film in Figure 4.3, it is not perfectly smooth. It has an observable thickness and rough texture. The thickness becomes more substantial (in terms of shape alteration) for the smaller spheres due to the higher ratio of film thickness to sphere diameter. As an example, one can compare Figure 4.3 (a) and (b) to (c) and (d).

Sphere Size Measurements	
Nominal Diameter (μm)	SEM Measured Diameter $\pm$ Standard Deviation (μm)
0.80	0.68$\pm$0.02
2.34	2.1$\pm$0.1
3.47	3.1$\pm$0.2
4.99	4.6$\pm$0.3

Table 4.1: A comparison of the nominal sphere size diameter as quoted by the manufacturer to our own SEM measurements. Several measurements were taken using the scale bar of the images and a ruler. The average and standard deviation of all measurements for each sphere size are shown here.

The film thickness is the same in all images (50 nm) but the sphere size is 5 μm in (a) and (b) and 0.8 μm in (c) and (d). Part of the mottled texture seen in Figure 4.3 (and all SEM images) could also be due to the gold coating of the sample that was required to reduce charging in the SEM. The gold coating was $\sim$15 nm as compared to the 50 nm nanocrystal film. The roughness and thickness of the film will be an important factor when considering loss mechanisms, as will be contamination that may have accumulated on the sample (as in Figure 4.1 (b) and (f) or Figure 4.2).

Using the SEM results, it was also possible to measure the approximate size of the spheres according to the scale bar in the images. The average and standard deviation of these measurements are shown in Table 4.1. The results showed that all spheres were about $10-15$ % smaller than their "sold as" diameter. The standard deviation of sphere diameter within each sample was confirmed to be less than 10 %, as was quoted by the manufacturer. However, occasionally spheres were observed that lay outside this range up to 50 % larger or smaller than the rest of the spheres. These will be labeled as "defects".

4.1.2 Array Structure

The fabrication technique was successful in producing long-range 2D arrays of spheres. Monolayers of close-packed hexagonal arrays were observed on all samples, as in Figure 4.4. However, some imperfections in the arrays existed due to the

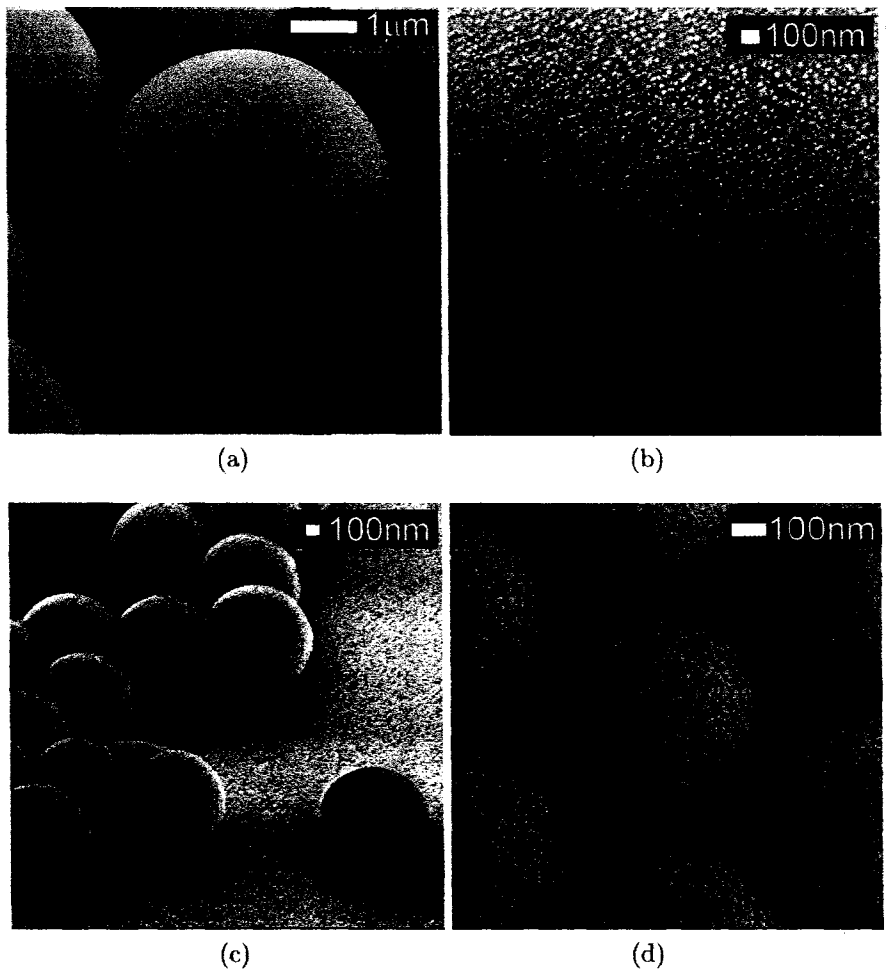

Figure 4.3: SEM images of the nanocrystal film texture. (a) and (b) show 5 μm spheres with a 50 nm film, where (b) is a close-up on the film ; (c) and (d) show 0.8 μm spheres with a 50 nm film.

presence of defect spheres. Figure 4.4 (a) shows a highly ordered SiO_x-coated array, while Figure 4.4 (b) shows a lower magnification image in which domain boundaries are visible.

The usual outcome of the drop-coating technique was a deposited area of $\sim$1 cm^2 of spheres. Arrays such as those in Figure 4.4 (b) covered the majority of this area. The rest of the deposited area consisted of more dispersed spheres that were not regularly ordered. This is where isolated spheres were found for taking single-sphere spectra. Since the nanocrystal film was deposited over the entire surface of the substrate, there were also areas of "film only" (i.e. areas of substrate where there were no spheres). The various areas of the sample (arrays, dispersed spheres, and "film only") were visible by eye, which was useful for collecting PL and images of any desired portion of the sample.

As a side note, some 3D arrays were also observed on the samples (as in Figure 4.5). These were found only on the smallest-sphere-size samples (0.8 μm), possibly due to the angle of the substrate during drop-coating of the spheres. If the angle was too high, the spheres could roll on top of one another while drying instead of forming a 2-dimensional monolayer. The 3D arrays resembled natural opals and appeared colorful to the eye due to dispersion effects. The ordered structure of opal effectively acts as a diffraction grating which disperses white light into various colours, depending on the viewing angle. Although the formation of the 3D arrays was unintentional and not the goal of the present work, the optical properties of 3D arrays of silica microspheres and nanospheres embedded by silicon nanoparticles was the focus of two previously mentioned articles in which WGMs were not observed [2, 96].

4.2 Photoluminescence Spectra

The main goal of this research was to examine how the luminescence of Si nanocrystals would be affected by the WGMs of the spheres. Therefore, in this section we present the results of many PL spectroscopy experiments. In all experiments, several spectra and images were collected to ensure the repeatability of the results. The background structure of the spectra will be discussed in Section 4.2.1, while sphere size and film thickness effects are presented in Sections 4.2.2 and 4.2.3, respectively.

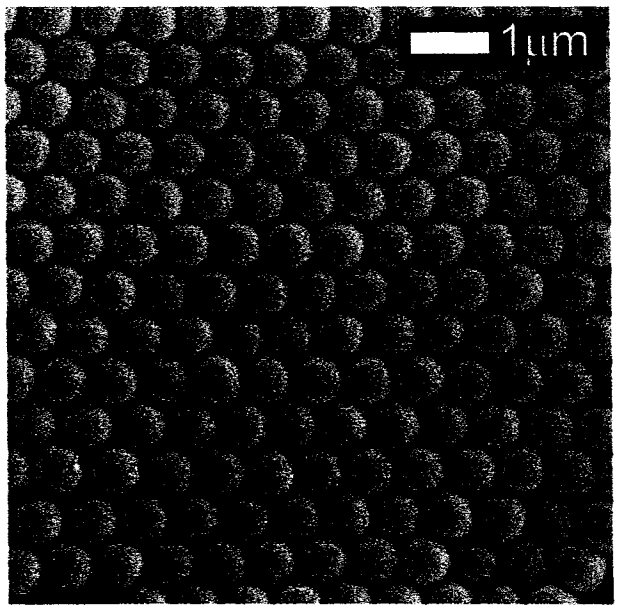

(a)

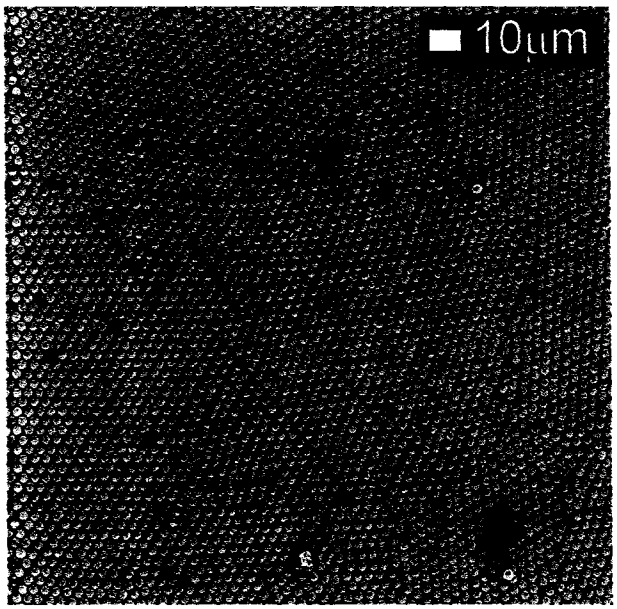

(b)

Figure 4.4: SEM images showing the hexagonal array structure: (a) a nearly perfectly ordered array of 0.8 μm spheres with a 50 nm coating; (b) a lower magnification image of an array showing domain boundaries. The spheres are nominally 3.5 μm with a 50 nm coating.

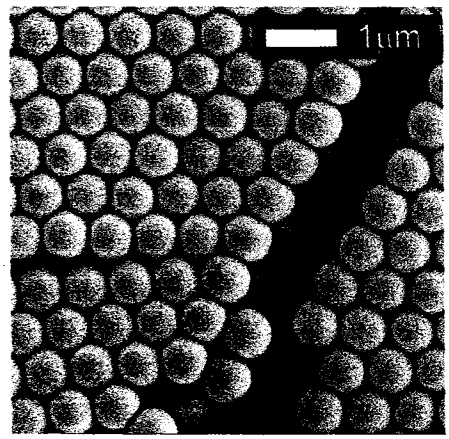

Figure 4.5: SEM image of a 3D array formed by 0.8 μm spheres with a 50 nm coating.

The mode structure from different areas of a single sphere will be discussed in Section 4.2.5. A detailed analysis of the mode structure follows in Chapter 5.

4.2.1 Background PL

All samples were luminescent when excited with a HeCd laser, and the majority showed clear evidence of WGMs. The WGMs appeared as oscillations atop a broad "background" that peaked between the wavelengths of 750 and 900 nm, depending on the sample. As an example, the WGM spectrum of a single 5 μm sphere coated with 100 nm film is shown in Figure 4.6. In this case, the background is centered around 825 nm. The main source of the background component was thought to be the PL from the nanocrystal film, but other possible sources will also be investigated in this section.

"Film only" PL spectra were taken in areas of the sample without any spheres, and the results are shown in Figure 4.7 (a) for the nominally $SiO_{1.2}$ films [28]. The spectra varied depending on the film thickness, but in general they peaked between 750 and 900 nm. In a recent report by Glover and Meldrum [28], it was found that as Si nanocrystal films were made thinner, the peak wavelength of the PL decreased (i.e. blueshifted), while the intensity increased. In the present work, the expected blueshift was observed for thinner films, however, the intensities of the film did not increase. The intensity of the 50 nm film was higher than that of the 100 nm

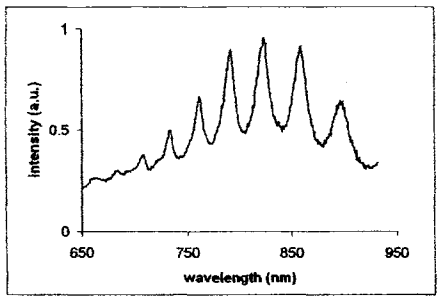

Figure 4.6: Single-sphere PL spectrum of a 5 μm sphere coated with 100 nm film. The WGMs oscillate atop a broad background centered around 825 nm.

film as expected, but instead of the 20 nm film having the highest intensity of the three thicknesses, it actually had the lowest. This discrepancy could be due to the unusually high oxygen pressure that occurred during the deposition of the 20 nm films (see Section 3.2.3), which may have caused a lower concentration of silicon in the 20 nm films than the other two film thicknesses. In any case, all films were sufficiently luminescent to permit an investigation of the WGMs.

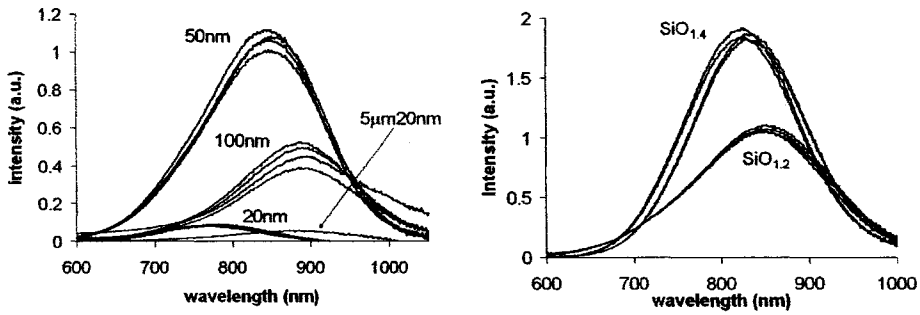

Figure 4.7: "Film only" PL spectra for: (a) three thicknesses of $SiO_{1.2}$ film, and (b) 50 nm films with two different compositions, $SiO_{1.2}$ and $SiO_{1.4}$. The four traces for each thickness or composition represent the samples made with the four sphere sizes from Bangs labs. For each thickness or composition, results were consistent except the "5μm20nm" spectrum which was redshifted with respect to the other three 20 nm film samples.

The four traces representing each thickness in Figure 4.7 (a) correspond to sam-

ples of the four sphere sizes from Bangs laboratories. The spectra were taken in areas without any spheres and the traces were compared in order to test the consistency of the film thickness and composition over all the samples. For each thickness the PL of the film was consistent for the four samples (i.e. the spectra had similar peak wavelengths and intensities), except for that of the "5μm20nm" sample. The PL of this particular film was less intense and redshifted compared to the rest of the 20 nm film samples.

Film composition is known to be an important factor in the PL spectrum and this was investigated by making another batch of samples with an $SiO_{1.4}$ film to compare to the $SiO_{1.2}$ batch. In previous experimentation, it was found that films of $SiO_{1.4}$ had a higher PL intensity than films of $SiO_{1.2}$. Indeed this trend is observed in the present data, as shown in Figure 4.7 (b) (the four traces for each film composition show the consistency of the film over the four sphere size samples). As well, the $SiO_{1.4}$ film had a PL spectrum that was blueshifted with respect to that of the $SiO_{1.2}$ film.

Although the composition of the film affects the background spectrum, it should play no role in the actual WGMs. The structure of the WGMs is dependent only on sphere size, shape, and refractive index. The composition of the film (i.e. the wavelength or intensity of light entering the sphere) is of no importance to the mode structure aside from the background. This shall be demonstrated in Section 4.2.3.

Aside from the nanocrystal film, it was possible that some background PL came from the spheres themselves. Such PL could be caused by luminescent impurities being distributed throughout the spheres during manufacturing. To test this, "blank" samples were made in which the spheres were annealed in the absence of the SiO_x coating. The ensemble PL from these spheres is shown in Figure 4.8. The peak wavelength and intensity varied for the four different sphere sizes, but no relationship was observed between the sphere size and the PL spectrum. The PL from the blank spheres was weak (in comparison to that of the nanocrystal films) and centered between 650 and 750 nm. The background in the WGM spectra is therefore a combination of the film spectrum and the "blank sphere" spectrum. The latter source is thought to have had a less significant contribution, since it was two to five times weaker than the PL from the 100 nm and 50 nm nanocrystal films. However, in the case of the 20 nm films, the "blank sphere" PL had about the same intensity

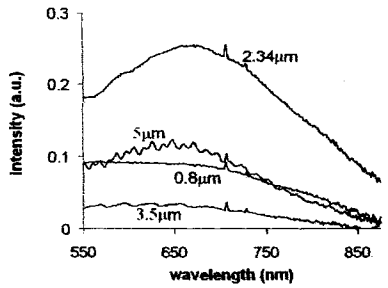

Figure 4.8: "Blank sphere" ensemble PL spectra for all four sphere sizes from Bangs labs. The spheres were annealed without any film.

as the "film only", so the blank spectrum is expected to play a larger role for those samples.

4.2.2 Whispering Gallery Modes: Sphere Size Effects

The effects of sphere size on the WGM spectra are shown in Figure 4.9. Figure 4.9 (a) shows ensemble spectra for the four sphere sizes with 100 nm film, while in (b) the corresponding single-sphere spectra are shown. The WGMs of the single-sphere spectra are considerably narrower than in the ensemble spectra, showing that the defects and sphere size distribution observed in the SEM broaden the modes observed in ensemble spectra.

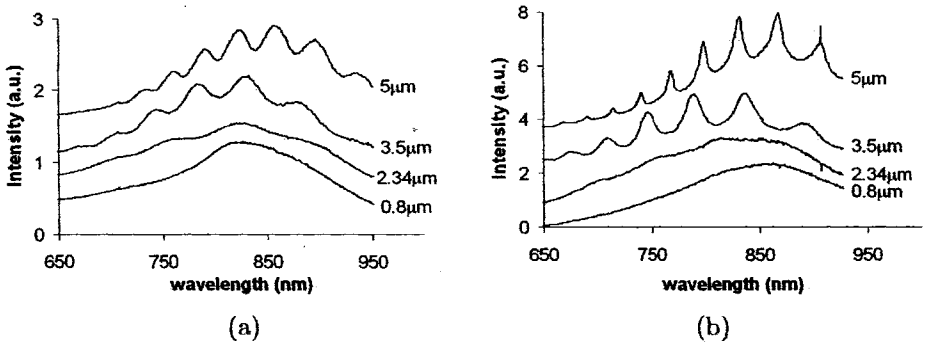

Figure 4.9: PL spectra for four different sphere sizes with 100 nm film: (a) ensemble spectra; (b) single-sphere spectra. Spectra are offset for clarity.

For the smallest spheres (0.8 μm) there is virtually no evidence of the WGM structure. The mode structure first becomes faintly observable for the 2.3 μm spheres. The observed relationship between sphere size and mode structure agrees well with theory. The peaks became more closely spaced (i.e. the free spectral range decreased) with increasing sphere size as discussed in Chapter 2. The peaks also became narrower with increasing sphere size, implying that larger spheres confine light better. This can be explained theoretically by the geometric optics picture of WGMs inside a sphere. Larger spheres have a larger ratio of sphere diameter to wavelength and so more wavelengths can fit inside the circumference of the sphere than in smaller spheres. Hence in a larger sphere the modes travel closer to the surface, with a smaller mode volume (i.e. the modes are more confined spatially). In this situation, light approaches the internal surface of the sphere at glancing angles so that diffraction losses are minimized [49]. This is one contributing factor to the lack of modes observed for the 0.8 μm spheres; the modes are simply too broad (or far apart) to be observed because the sphere is so small. Another important factor is the high ratio of nanocrystal film to sphere diameter (100 nm compared to 800 nm), which leads to a higher aspect ratio.

To estimate the quality factor, the modes were normalized by subtracting the background from the spectrum. This was done by selecting points along the background (i.e. the lowest points between the modes) and interpolating between them. A cubic spline interpolation method was used in Matlab to predict values at intermediate points and find a 1D function underlying the data. Then the interpolated function was subtracted from the spectrum. The full-width-at-half-maximum and peak wavelength was determined from the normalized modes in order to estimate the Q factors (Figure 4.10). Due to inaccuracies in selecting the exact lowest points between the modes to find the background, some points of the normalized spectrum were given a negative intensity as shown in Figure 4.10. The dip below zero was always slight, but it did produce some difficulty in determining the FWHM for modes that were uneven at the bottom. In this case, the FWHM was always measured from the lowest point between the modes. For each peak between 700 and 900 nm, Q was found and the average was taken over all peaks. Using this method the average Q factors for the ensemble spectra were Q = 22, 37, and 46 (for the 2.3, 3.5, and 5 μm spheres, respectively). For the single-sphere spectra, Q factors were Q = 38,

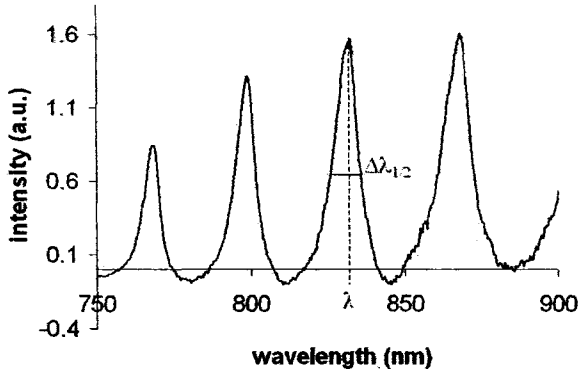

Figure 4.10: Normalized single-sphere spectrum (i.e. with background removed) for a 5 μm sphere with 100 nm film. The Q factor was estimated by measuring the full-width-at-half-maximum ($\Delta\lambda_{1/2}$) and the peak wavelength (λ) of each mode.

48, 121 (for the 2.3, 3.5, and 5 μm spheres, respectively). The Q factor was greater for the single-spheres than the ensembles, and increased with sphere size.

Although this method produces better formed spheres as compared to previous investigations using ion implantation, the Q factors are still rather low. As seen in the SEM images, the nanocrystal film has roughness, imperfections, and contamination on the surface. These, as well as water vapor (which is assumed to be present as well) are known to seriously lower the Q factor [30, 85, 20, 19]. However, shape effects due to the film itself are expected to be among the most significant loss mechanism in these samples. As shown in the SEM images, the coating represents a significant fraction of the total sphere diameter, especially in the case of the 0.8 μm spheres. In order for well formed WGMs to occur inside a sphere, the sphere should be perfectly symmetrical. Any deformation of the sphere's shape will cause a lack of confinement of light and therefore broaden the modes. As an example, recall the deformed "muffin-shaped" microspheres which produced virtually no WGMs in previous work [70].

4.2.3 Whispering Gallery Modes: Film Effects

To determine effects of the nanocrystal film on the resulting WGM spectrum, two factors were considered: composition and thickness. As mentioned in Section 4.2.1,

the mode structure depends only on the size, shape, and refractive index of the sphere. So although film thickness may affect the WGMs (due to shape changes), film composition should not. To illustrate this, single sphere spectra were taken for 5 μm spheres with 50 nm of $SiO_{1.2}$ and 5 μm spheres with 50 nm of $SiO_{1.4}$. The change in composition caused no change in the peak wavelengths or mode structure of the WGMs (Figure 4.11 (a)).

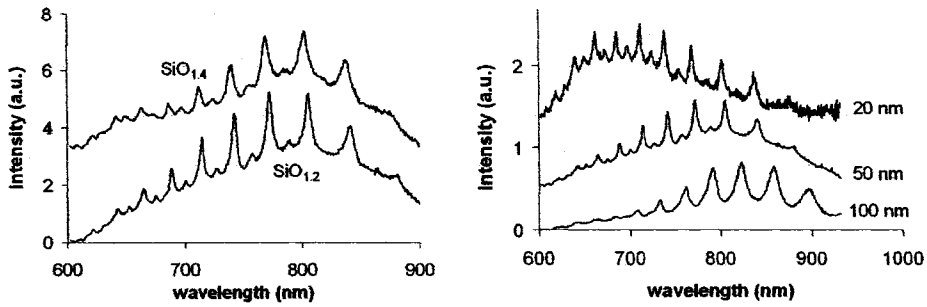

Figure 4.11: Effects of the nanocrystal film composition and thickness on PL spectra: Single-sphere spectra for 5 μm spheres with (a) 50 nm films of two different compositions, $SiO_{1.2}$ and $SiO_{1.4}$, and (b) three different thicknesses of $SiO_{1.2}$ film. Spectra are offset for clarity.

In order to investigate possible effects of the nanocrystal film on the Q factors of the microspheres, sets of samples were produced with film thicknesses of 100 nm, 50 nm and 20 nm. Figure 4.11 (b) shows the single-sphere PL for 5 μm spheres with three different film thicknesses. On decreasing the film thickness from 100 to 50 nm, the modes became sharper and the initially single peaks split into two narrower ones. These two peaks represent the TE and TM polarizations of the modes and, as we shall see in the next chapter, the more intense modes are due to the TM polarization. When decreasing the film further from 50 nm to 20 nm, the modes became still sharper.[2] The reason that the TE and TM modes are resolved for the 20 nm and 50 nm films but not the 100 nm film is clear. By adding the film thickness, the aspect ratio of the structure changes and hence the Q factor

[2]the significant difference in background structure for the 20 nm film in Figure 4.11 (b) is likely due to the unusual composition of that one film, as mentioned in Section 4.2.1.

decreases, broadening the modes. The modes are broadest for the thickest film and the closely spaced TE and TM modes simply merge into one peak as discussed in Chapter 2. Average Q factors for the spectra in Figure 4.11 (b) were found for the TM modes between 650 to 850 nm. The results showed that the Q factor increased as the film thickness decreased: $Q = 82$ (100 nm coating), 156 (50 nm coating), and 173 (20 nm coating).

4.2.4 20 Micron Spheres

The highest Q factors so far obtained from the 5 μm spheres with 20 nm film were $\sim$200. Although higher than previous work with Si nanocrystals and microspheres, these numbers are still low compared to results for Si nanocrystals in planar microcavities (Q =$\sim$500) [40, 39]. In order to investigate the possibility of higher Q factors, the experiments were repeated using microspheres with a nominally 20 μm diameter.

The nominally 20 μm spheres were ordered from a different company (Kisker) than the other four sets (Bangs Labs), and imaging showed that the size distribution of these larger spheres was as high as 50% (eg. see Figure 4.12 (a)). Spheres ranged in size between $\sim$10 to 30 μm. Therefore the spheres did not self-organize into ordered arrays as they did with the other sizes, and it was difficult to find several spheres of the same size to analyze and compare. When collecting single-sphere spectra, the spheres that appeared to be largest were always chosen for consistency (and to find the highest possible Q factors). An example single-sphere spectrum for the nominally 20 μm spheres is shown in Figure 4.12 (b). The modes of these large spheres were sharp and closely spaced, with average Q factors around 500.

The background spectrum peaked between 650 – 800 nm (on average about 100 nm less than the spheres from Bangs Labs). This makes sense when looking at the separate components of the background spectra. The "film only" PL spectra also peaked between 650 – 800 nm (Figure 4.12 (c)), while the blank PL spectrum (for spheres annealed without any film), peaked around 600 nm (Figure 4.12 (d)). The "film only" data was consistent with the previous samples. The composition was $SiO_{1.4}$ and was blueshifted with respect to those with composition of $SiO_{1.2}$. This is the same trend shown earlier in Figure 4.7 (b). The 50 nm film had the highest intensity, while the thinnest film (5 nm) had the lowest (as was the case in

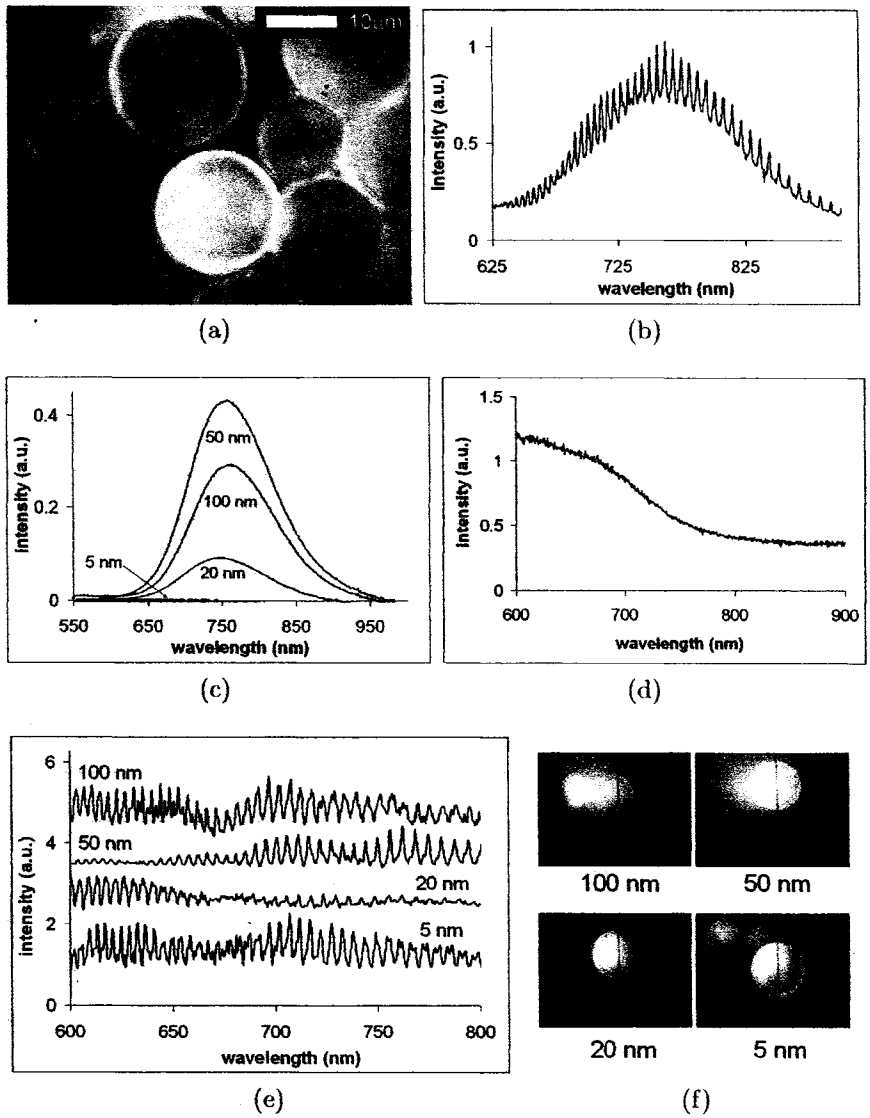

Figure 4.12: PL results for the nominally 20 μm spheres: (a) Fluorescence image of the spheres coated with 100 nm film. The size distribution of these spheres was large. (b) Single-sphere PL spectrum of a sphere coated with 50 nm film. (c) "Film only" PL spectra for the four film thicknesses used to coat the spheres. (d) "Blank" PL spectrum for a single sphere annealed without any film. (e) Normalized single-sphere PL spectra for spheres coated with various film thicknesses. Spectra are offset for clarity. (f) Images of the spheres (aligned with the spectrometer slit) corresponding to the spectra in (e).

Figure 4.7 (a)).

The effects of film thickness on the WGM spectrum of the 20 μm spheres is shown in Figure 4.12 (e). Each spectrum corresponds to a single sphere with a different film thickness. The modes have been normalized in order to see the structure more clearly. The mode structure in this case does not show any clear trend with increasing film thickness. Average Q factors for all peaks between $600 - 750$ nm were taken for all spectra. Q factors were found to be 448 (100 nm coating), 458 (50 nm coating), 389 (20 nm coating), and 610 (5 nm coating). However, due to the large size distribution of these spheres, it was difficult to find four equally sized spheres to use for comparing film thickness effects. So, although the 5 nm coating produced the highest Q factors in this case, it is thought that this is at least partly due to that particular sphere being largest of the four (Figure 4.12 (f)). Theoretical approximations of the four sphere diameters based on the mode spacing in the spectra (as will be done in the next chapter) showed that the sphere diameters in Figure 4.12 (e) were approximately 24 μm (100 nm coating), 25 μm (50 nm coating), 22 μm (20 nm coating), and 26 μm (5 nm coating). Comparing these values to the calculated Q factors shows that the Q factors increased with increasing sphere size.

The highest individual Q factors that were observed from single peaks of the 5 nm coated sample spectra were around 1500. However, these values may be limited by the spectrometer's resolution, which is $\sim$1 nm. At this resolution, modes with Q factors greater than $\sim$1500 will not be resolvable. However, even with this limitation, the measured Q factors are higher than those for recent reports of Si nanocrystals inside planar microcavities [40, 39].

4.2.5 PL from a Single Sphere

In general the luminescent spheres appeared ring-shaped when viewed from above, as shown in Figure 4.13. This is consistent with theoretical calculations of the electromagnetic field of a light emitter in or near a spherical cavity, which is highest near the surface [7, 91]. As discussed in Chapter 2, the WGMs circle the equator of the sphere close to the surface. In this case, light enters the sphere in random directions from the nanocrystals covering the entire upper hemisphere. Hence the WGMs circle the sphere in all directions. If the sphere is viewed from above, the line of sight intersects more of the mode volume near the edges of the sphere (as

opposed to the center), and hence the sphere appears ring-shaped. As the size of sphere is decreased into the sub-wavelength regime, the emission becomes closer to the bulk case and so the ring structure becomes less-pronounced [73, 91]. In the fluorescence images the ring structure was clearly observable for the 20 μm spheres (as shown previously in Figure 4.12 (a)), 5 μm spheres (Figure 4.13 (a)), 3.5 μm spheres (Figure 4.13 (b)), and 2.3 μm spheres (Figure 4.13 (c)). In the images of the 0.8 μm spheres, the ring-like structure was not observed (Figure 4.13 (d)).

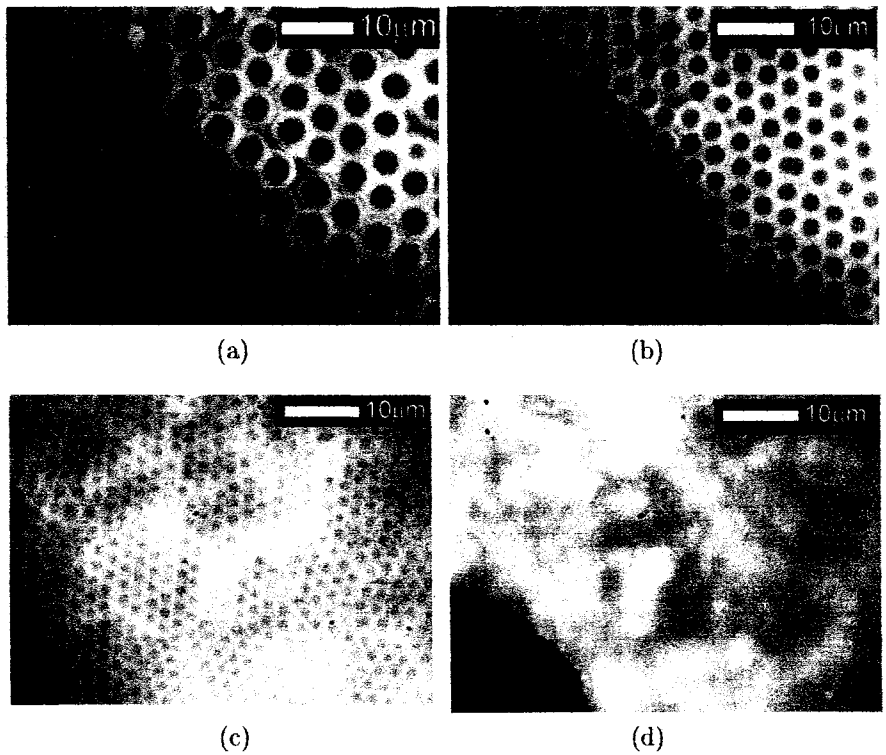

Figure 4.13: Fluorescence images of arrays of spheres showing the ring-like structure of the luminescence. All samples have 100 nm film coating, and the nominal sphere diameters are: (a) 5 μm; (b) 3.5 μm; (c) 2.3 μm; and (d) 0.8 μm.

Single spheres were subsequently aligned with the entrance slit of the spectrometer, and the PL spectrum was cropped from different regions of the sphere's intersection with the slit: the top edge, center, and bottom edge of the sphere (Figure 4.14). There were obvious differences in the mode structure between the outer ring-like por-

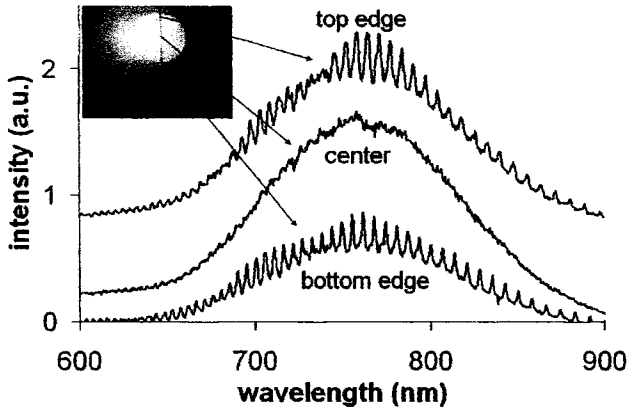

Figure 4.14: Single-sphere PL spectra from different areas of a 20 μm sphere coated with 50 nm film. The inset shows the sphere aligned with the entrance slit of the spectrometer. Spectra are offset for clarity.

tion and the center of the sphere. The WGMs were well developed at the edges of the sphere, but there was little evidence of mode structure in the spectra obtained from the sphere centers. This was consistently observed for all single-sphere spectra. The "center" in this case does not actually refer to the center of the sphere (where no modes would be expected), rather it refers to the center of the sphere's intersection with the slit from the top view, so that all modes traveling vertically (with respect to the horizontal substrate) intersect this point. The lack of mode structure detected in this region shows that there was loss in the modes traveling perpendicular to the substrate compared to those traveling parallel (compare 'topview" vs. "sideview" in Figure 4.15). The vertical modes intersected both the contact point of the sphere with the substrate and the thickest portion of the nanocrystal film. Both of these factors were investigated.

The nanocrystal film appeared not to be responsible for the weak structure in the sphere center spectra. This was determined by comparing "edge v.s. center" spectra (similar to Figure 4.14) for 5 μm spheres having film thicknesses of 100 nm, 50 nm, and 20 nm (Figure 4.16 (a), (b) and (c), respectively). If film thickness was a cause for mode loss in the center due to the increase in sphere ellipticity, than the center modes should have weakened with increasing film thickness. The results were inconsistent with this idea as shown in Figure 4.16.

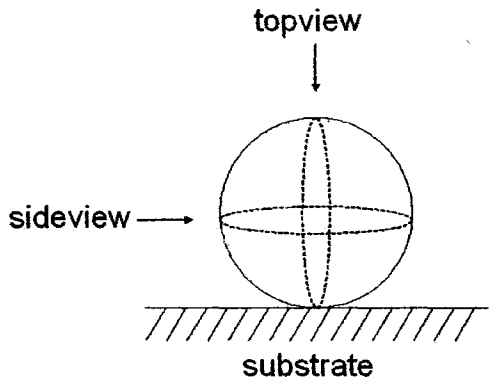

Figure 4.15: The two different viewing angles of the sphere with respect to the substrate. Arrows represent the direction that PL spectra were collected from. In the topview, WGMs in the center of the sphere were lossy, while in the sideview they were not.

The effects of the contact point of the sphere and the substrate were tested by placing the substrate on its side (i.e. perpendicular to the original direction) and analyzing sphere spectra in the same way as before (Figure 4.15). With this set-up, the contact point of the sphere and substrate no longer intersected the slit, and so it was not expected to affect the mode structure in the center. As discussed in Chapter 3, this experiment presented a challenge in that only spheres that were at the very edge of the substrate could be analyzed, and these were scarce. In total six spheres were found on the "5μm20nm" sample, and "edge v.s. center" spectra were collected. The difference between the spectra in this sideview direction (Figure 4.16 (d)) compared to the previous topview (Figure 4.16 (c)) is striking. In all sideview spectra, the mode structure was well developed and strong in the center, supporting the hypothesis that the contact point with the substrate is a major source of loss.

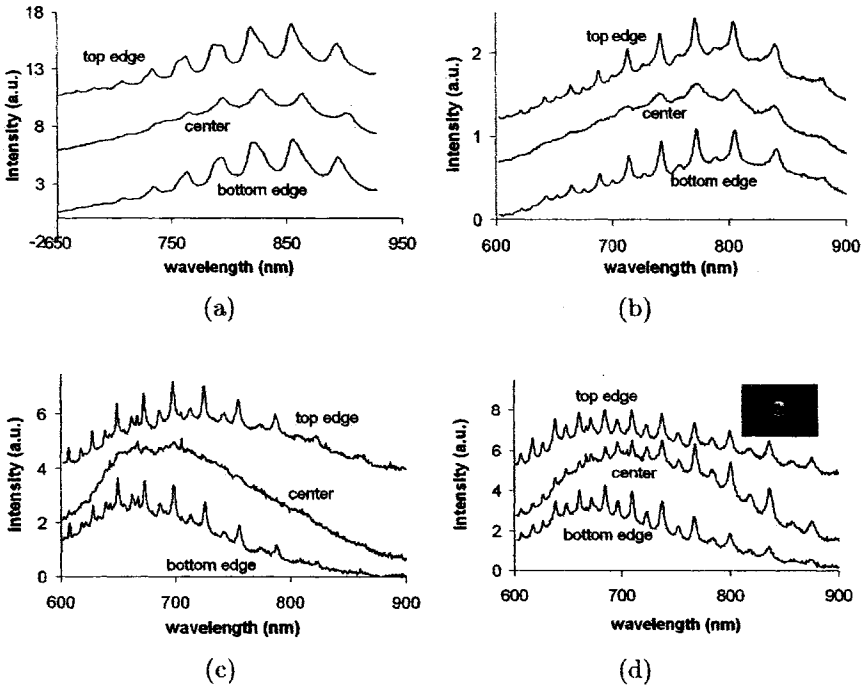

Figure 4.16: "Edge v.s. center" spectra for 5 μm spheres with film thicknesses of: (a) 100 nm; (b) 50 nm; (c) 20 nm and (d) 20 nm (sideview). In (a), (b), (c) the spectra were collected in the usual viewing direction. In (d) the substrate is propped on its side, so that the contact point of the sphere with the substrate is on the side of the sphere when viewed in the microscope, as shown in the inset (reflection image). In each figure, spectra are offset for clarity.

Chapter 5

Analysis

The purpose of this chapter is to compare the experimental results to the theoretical predictions given in Chapter 2. The results are compared to theory given mainly in the following references: Hill and Benner, 1988 [34], Lu et al., 1992 [58], Lefèvre-Seguin, 1999 [55], Schiller, 1993 [71], and Schiller and Byer, 1991 [72]. The results are also compared to theoretical models generated by the computer program Mieplot. Mieplot uses calculations from standard Mie scattering theory to produce the WGM spectrum for a sphere of given size and refractive index.[1]

Several spectra were chosen for comparison to theory, and the chapter begins with an overall comparison of these spectra (Section 5.1). It continues with results of a number of calculations that compare the spectra to theory. The main results of these calculations are the values of the order numbers n, l, and m (Section 5.2), quality factor Q (Section 5.3), rate enhancement η (Section 5.4), and approximations for the diameter d based on the free spectral range Δx_{FSR} (Section 5.5). For each spectrum, calculations were done for every peak in the wavelength range 650 – 800 nm and then the average was taken to determine the overall value for that spectrum.

5.1 Overall Comparison of Spectra

All spectra used in the comparison of experiment to theory are shown in Figure 5.1. The background has been removed from each spectrum for a clearer comparison.

[1]The program was written by Philip Laven, and is available as freeware at www.philiplaven.com

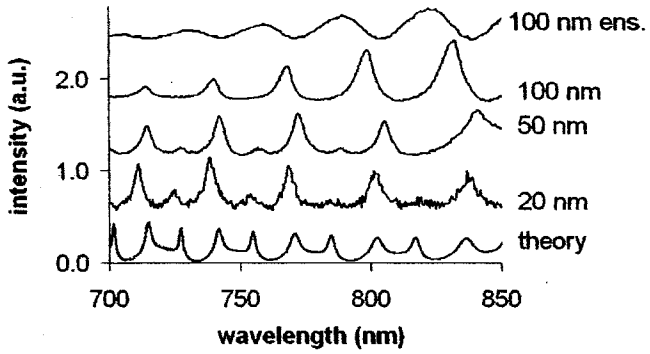

Figure 5.1: Normalized spectra used in the analysis. All spectra are from 4.99 μm spheres, and are named according to their film thickness in nanometers. All are single-sphere spectra except "100 nm ens." which is an ensemble spectrum.

For a sample of the experimental data, four spectra were chosen for the comparison from the 4.99 μm diameter spheres: "100 nm ens", "100 nm", "50 nm", and "20 nm". The latter three are single-sphere spectra, while the first is an ensemble spectrum. They are named according to the thickness of their film in nanometers. A theoretical spectrum from Mieplot, "theory", is also included as a reference. This theoretical spectrum was calculated for a 4.99 μm diameter sphere surrounded by air, at a scattering angle of 0^o. The refractive index was 1.37 and was assumed to be constant with wavelength (i.e. the sphere was non-dispersive).

Aside from differences in mode structure caused by film thickness, theoretically the spectra should all be the same. Although they were similar, a slight shift in peak wavelengths was observed between the spectra. This was expected since the spheres had a standard deviation of $\sim$10 % in the diameter. Since size, shape, and refractive index are the defining factors of the resonance wavelengths [34], a small size difference could easily have caused the observed shift from one spectrum to the next. For example, calculations using Equation 2.14 (as in the next section) showed that a mode could be shifted by over 100 nm by changing the diameter from 4.5 to 5.5 μm.

5.2 Indexing the Modes

The first analysis of the data was to index the modes with their order numbers n, l, m, and their polarization (TE or TM). As a reminder and quick reference for the reader: n = **angular order number (or mode number)**, l = **radial order number (or order number), and** m = **azimuthal order number (or magnetic number)** (see Section 2.2.3). For perfect spheres (i.e. with no ellipticity), modes are degenerate with respect to m [34]. For the present discussion, it was assumed that the spheres were approximately spherical, and hence m was neglected in the indexing of the modes.[2]

The order number, l, corresponds to the number of field maxima in the radial direction through the sphere. Modes with high l values extend more towards the center of the sphere than those with low l values. Whispering gallery modes are confined near the inner surface of the sphere, and so they correspond to the lowest l values [77]. It was therefore assumed that the observed peaks in Figure 5.1 were the $l = 1$ and $l = 2$ modes.

To test this assumption, the theoretical spectra from Mieplot and the modal positions calculated via Schiller's asymptotic expansion [71] were compared. A program was written in Matlab to calculate the expansion using Equation 2.14. Resonance locations could be calculated for any given n, l, and polarization, and for any given refractive index of sphere and surrounding medium (see the appendix for the full code of the Matlab program). The program was used for a sphere of refractive index $N = 1.37$ surrounded by air ($N = 1$) to find all TE and TM resonance locations with $l = 1$ and $l = 2$ for n between 1 and 144. The range of n values was approximated using Equation 2.12 ($2\pi a/\lambda < n < 2N\pi a/\lambda$) for wavelengths of $600 - 900$ nm and sphere diameters of $1 - 20$ μm with refractive index of $N = 1.37$.

In Figure 5.2, the evolution of the modes with increasing sphere size is shown. The $l = 1$ and $l = 2$ mode locations are plotted against corresponding theoretical spectra from Mieplot for spheres increasing in diameter from 3 μm to 20 μm. According to theoretical predictions, the $l = 1$ modes are the first to appear in the

[2] If the sphere has some ellipticity, the frequency shift Δf between modes differing only in m values is related to the ellipticity e by $\Delta f/f = e/n$, where n is the mode number [55]. In the present work, the ellipticity due to the film was less than 2%, hence any mode splitting due to ellipticity was expected to be unobservable (and indeed no such splitting was observed).

spectrum for small spheres [34]. Then, as size is increased, these modes narrow and the $l = 2$ modes appear. Each mode eventually narrows so much with increasing sphere size that it becomes no longer resolvable in the spectrum. This trend is apparent in Figure 5.2 (a) - (e) as size is increased between 3 to 7 μm. In (a) and (b) (3 and 4 μm), the only resonances that appear are $l = 1$ modes. In (c) and (d) (5 and 6 μm) the $l = 1$ modes begin to narrow and the $l = 2$ modes are just slightly resolvable as small broad maxima between the larger peaks. Finally, in (e) (7 μm) the $l = 1$ modes have almost completely disappeared (some very narrow ones are still visible in the spectrum) and the $l = 2$ peaks are very much resolvable. In (f) the Mieplot calculation for a 20 μm sphere is given as an example of how complex the modes become for a relatively large sphere. At this size, many higher order modes have appeared in the spectrum.

From Figure 5.2 (c) it was determined that for a 5 μm sphere, only the $l = 1$ modes appear in the spectrum, and the TM resonances have a higher intensity than the TE resonances (but this is not the case for all sphere sizes, as in (b) for example). So, to index the modes of the experimental spectra, one of them ("50 nm") was plotted along with a Mieplot spectrum and the $l = 1$ modes calculated using Matlab for a 4.99 μm sphere with refractive index of $N = 1.37$. For comparison purposes the background was subtracted from the spectra. The result is shown in Figure 5.3 (a). The experimental spectrum agreed well with the theoretical models in terms of peak wavelengths and relative intensity of TE and TM modes. The mode indexing of the experimental spectrum is clear from this comparison. Again it was confirmed that the TM modes had the highest intensity. TE and TM modes of the same n and l were neighboring each other, and n decreased with wavelength as expected from the discussion in Section 2.2.3. In Figure 5.3 (b), the same experimental spectrum is shown again (this time without background removed) with formal indexing of the modes in standard notation a_n^l (TE modes) and b_n^l (TM modes).

5.3 Quality Factor

The quality factor of each spectrum in Figure 5.1 was found from the normalized modes using $Q = \lambda/\Delta\lambda_{1/2}$ where λ is the peak wavelength, and $\Delta\lambda_{1/2}$ is the full width half maximum of that peak. Average values for each spectrum are shown in

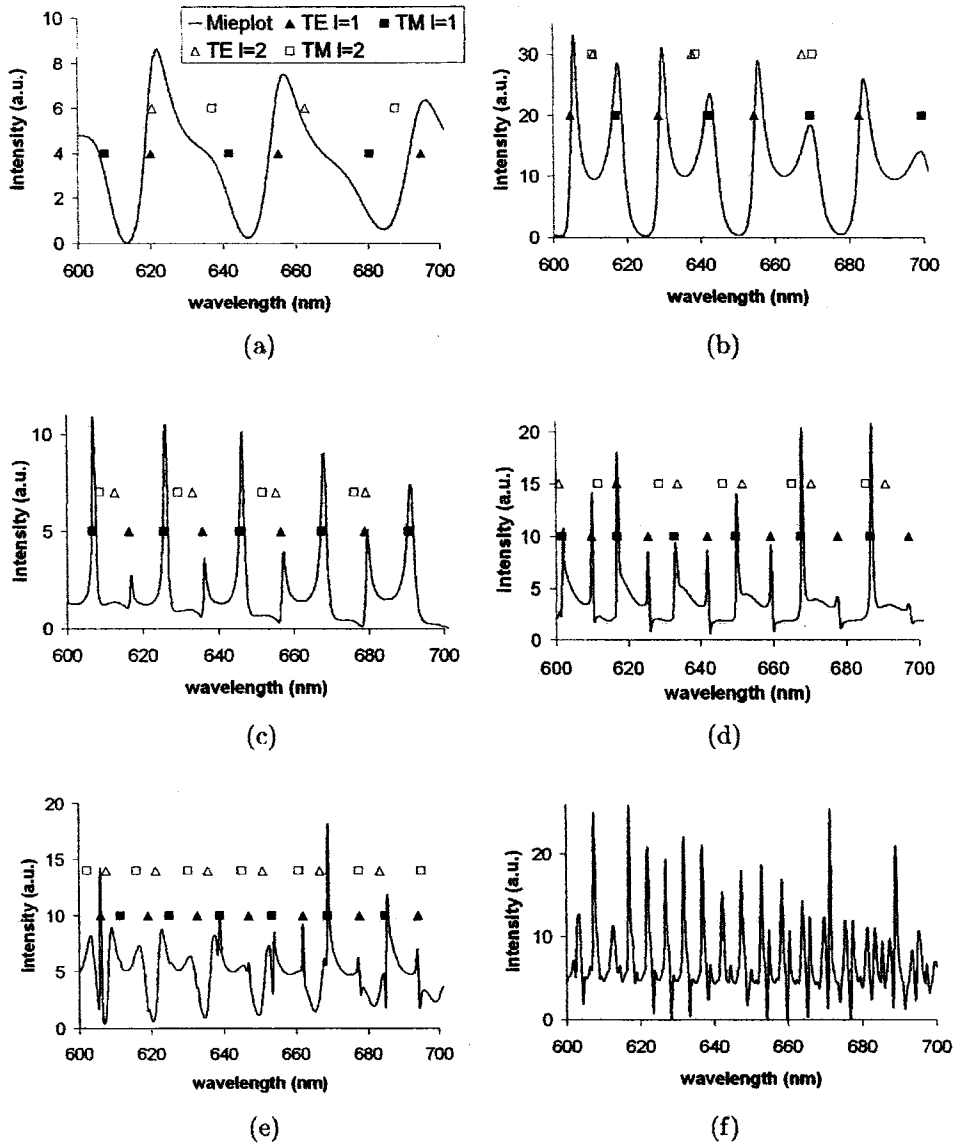

Figure 5.2: Evolution of the modes with increasing sphere size. Normalized theoretical spectra from Mieplot are plotted against predicted resonance locations according to Schiller [71] (triangles and squares) for spheres of diameter: (a) 3 μm; (b) 4 μm; (c) 5 μm; (d) 6 μm; (e) 7 μm; (f) 20 μm. The legend is the same as in (a) for all graphs.

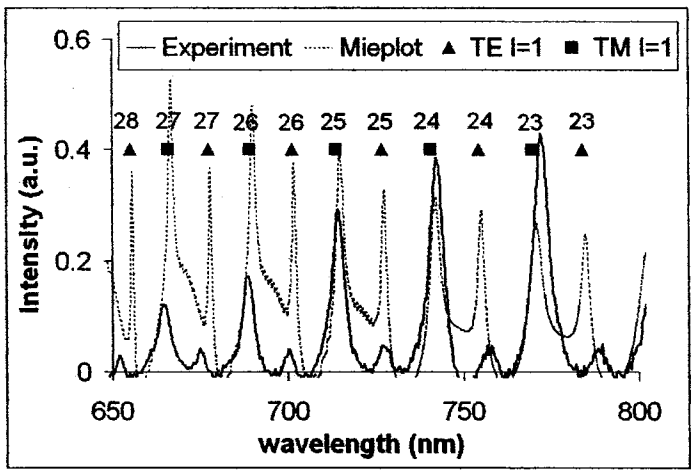

(a)

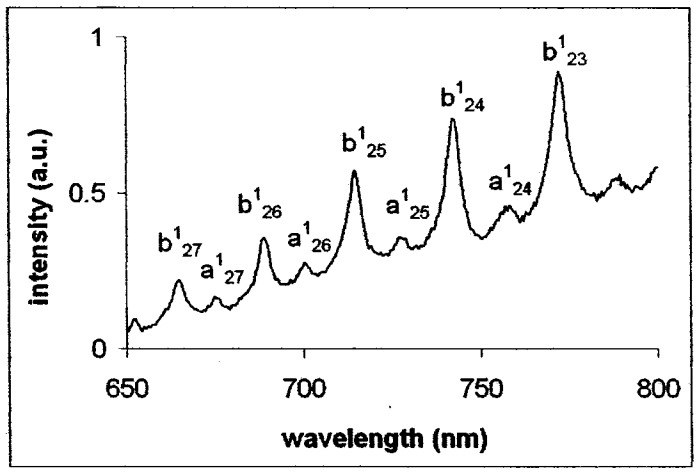

(b)

Figure 5.3: Indexing the modes of an experimental single-sphere spectrum from a 4.99 μm sphere with 50 nm film. (a) The normalized experimental spectrum plotted against Mieplot's theoretical spectrum and Schiller's resonance locations [71] (triangles and squares). The numbers above the Schiller positions represent the corresponding angular mode number n. (b) The same experimental spectrum again (without background removed), indexed according to standard notation a_n^l (TE modes) and b_n^l (TM modes).

Table 5.1. Quality factors for the TM peaks were on the order of $Q = 100 - 150$ for the experimental data, whereas for the TE peaks Q was around $170 - 230$. The TE peaks (i.e. the smaller peaks) had higher Q than those of the TM peaks (larger peaks). TM modes are known to extend slightly more outside the sphere compared to the TE modes, hence TE polarized modes are associated with more efficient confinement of light and have slightly higher Q factors [77].

The quality factors of the theoretical spectrum were $Q = 213$ for the TM modes and $Q = 392$ for the TE modes. These values are higher than those of the experimental spectra, due to the numerous loss mechanisms in the samples. The quality factor tended to decrease with increasing wavelength in most cases, and this relationship was most clearly seen in the theoretical spectrum. As discussed in Hill and Benner, 1988 [34], the resonance peaks become narrower as size parameter is increased. Since size parameter is inversely proportional to wavelength, resonance peaks should become broader (i.e. Q should decrease) with increasing wavelength.

5.4 Rate Enhancement

As discussed in Chapter 2, for a sphere of refractive index N, quality factor Q and size parameter x, the rate enhancement is $\eta = \sqrt{2}N^2Q/x^{3/2}$ (Equation 2.19) under the assumptions that (1) Q is low, (2) $Q << Q_{ab}$, and (3) $n \approx x$. According to the previous section assumption (1) is satisfied; Q factors are low, relatively speaking (as an example, "high Q" usually refers to values of at least 10^4).

Assumption (3) is also satisfied since Q factors were low. Each mode has a corresponding mode number n that is between $n_{min} = x$ and $n_{max} = Nx$. When Q values are low, it is reasonable to assume that n is closer to x rather than Nx [58]. A physical interpretation of n being close to n_{min} means that the light approaches the inner surface of the sphere at relatively high angles (close to the critical angle) and so it is not confined as close to the surface as it would be in the case of $n = n_{max}$ and not as many wavelengths can fit around the sphere's circumference.

To consider assumption (2), it was recalled that Q_{ab} is the absorption factor given by $Q_{ab} = 2\pi N/\alpha\lambda$ [58]. For spheres without any impurities, $\alpha = 0$ so that $Q_{ab} \rightarrow \infty$, and assumption (2) is satisfied. The spheres in this experiment most likely had impurities, as suggested by the PL coming from "blank" spheres that was

Calculations for WGMs of spectra in Figure 5.1				
TM modes				
Spectrum	Q	η	d (μm)	δd (%)
theory	213	50	5.23	5
20 nm	152	36	5.04	1
50 nm	148	36	5.04	1
100 nm	131	31	5.35	7
100 nm ens.	104	26	5.23	5
TE Modes				
Spectrum	Q	η	d (μm)	δd (%)
theory	392	90	5.29	6
20 nm	168	40	5.00	0
50 nm	229	53	4.97	2

Table 5.1: Average calculated values for all modes between $650 - 800$ nm for the spectra in Figure 5.1: quality factor Q, rate enhancement η, diameter d, and corresponding percent difference δd from the expected value of 4.99 μm. The spectra "100 nm" and "100 nm ens." are not included in the "TE Modes" section since they did not display any TE peaks.

shown in Section 4.2.1. The actual value of α was unknown. However, for the sake of the calculation, it was assumed that the spheres are pure enough for assumption (2) to be satisfied so that Equation 2.19 could be used to get a rough idea of the rate enhancement.

Average values of the rate enhancements were calculated according to Equation 2.19, and are shown in Table 5.1. Rate enhancements of the experimental spectra were found to be around $\eta = 25 - 35$ (TM modes) and $\eta = 40 - 55$ (TE modes). These are low values, relatively speaking. Theory predicts that enhancements for a spherical cavity can be over 1000 [18, 17, 15]. Since the enhancement is proportional to Q and is another measure of how well the light is confined inside the sphere, low η values were expected. As in the case of the Q factor, the enhancement factor was lowest for the "ensemble" sample and generally increased for samples with decreasing film thickness. As well, the TE modes had higher enhancements than the TM modes. The rate enhancement could, in principle, be obtained from a direct measurement of the luminescence lifetimes at the resonance wavelengths. This will be a subject of future investigation for this study, as the equipment will be acquired over the next few months that should enable this type of experiment.

5.5 Free Spectral Range

In this section, the mode structure of the experimental results is further compared to theoretical predictions in terms of the free spectral range. As discussed in Section 2.2.3, there are three approximations for calculating the theoretical free spectral range of the WGMs (Equations 2.16, 2.17, and 2.13). In order to make a comparison with a directly observable parameter, the equations were rearranged to find the theoretical diameter of the sphere based on the mode spacing of the experimental spectra. As an example, Equation 2.16 is used below to calculate the diameter based on the experimental free spectral range, and compare this to the "expected" value (as given by Bangs Labs) of 4.99 μm.

Equation 2.16 gives the free spectral range between successive peaks of the same polarization, m, and l values (differing only in n) in terms of size parameter x: $\Delta x_{FSR} \approx \tan^{-1}[(N^2-1)^{1/2}]/(N^2-1)^{1/2}$ [34, 58]. Using $N = 1.37$ for the silica spheres, Equation 2.16 gives a theoretical free spectral range of $\Delta x_{FSR} = 0.80$.

An expression for d in terms of $\Delta\lambda_{FSR}$ can then be found using $x = 2\pi a/\lambda = \pi d/\lambda$, so that $\Delta x \approx \pi d(\Delta\lambda/\lambda^2)$, and

$$d \approx \frac{\lambda^2 \Delta x_{FSR}}{\pi \Delta\lambda_{FSR}} \tag{5.1}$$

where λ is the peak wavelength, and $\Delta\lambda_{FSR}$ is the difference in wavelength between neighboring TE peaks or neighboring TM peaks (i.e. free spectral range in terms of wavelength). This expression has been quoted with respect to fluorescent spheres [58].

Equation 5.1 was used with $\Delta x_{FSR} = 0.80$ and the experimental values for λ and $\Delta\lambda_{FSR}$ as observed on the spectra to determine values for d (see Table 5.1). For the experimental spectra, the agreement was good between the calculated diameters and the expected value. Average calculated diameters were in general slightly higher (between $4.97 - 5.35$ μm) than the actual quoted diameter from Bangs Labs of 4.99 μm. Average calculated percent differences between the expected value and the calculated value are shown in Table 5.1. For the experimental spectra, the percent difference ranged from $0 - 7$ %. The worst agreement (i.e. the highest calculated diameters) were for the 100 nm coated sample (both single sphere and ensemble spectra). Values calculated for the other two samples agreed within 2 % difference to the expected diameter. Therefore, the experimental results agree reasonably well with theory. The slight differences observed are most likely due to the fact that dispersion has not been taken into account in these calculations (the refractive index N was assumed to be constant with wavelength since the actual relationship was unknown).

Chapter 6

Conclusions

This thesis presents a new method for incorporating silicon nanocrystals into microspheres that has demonstrated strong whispering gallery modes in the spheres. Silicon nanocrystal films were deposited by electron-beam evaporation onto silica microspheres and the resulting optical properties were studied. The microspheres maintained their spherical shape during the sample-making process, unlike previous attempts using ion implantation where there was deformation. [70, 82]. The microspheres were successfully patterned into long-range 2D arrays. The spheres produced visible luminescence that peaked between the wavelengths of $650 - 950$ nm and was intensified at resonance wavelengths corresponding to the WGMs of the sphere. The peak wavelengths of the WGM spectra agreed well with predictions based on Mie scattering theory. The modes were indexed with the appropriate quantum numbers, and the diameter of the sphere was calculated based on the free spectral range of the modes.

The fluorescence appeared as a thin ring near the edge of the sphere, showing that the electromagnetic field intensity was highest near the surface as theory predicted [7, 91]. The mode structure was sensitive to the position inside the sphere. Spectra from the central portion showed weak WGMs when compared to the spectra from the edges of the sphere. This was caused by scattering from the contact point of the sphere and the substrate, as was determined by analyzing the sphere from the "sideview". In this viewing angle the contact point was no longer in the center, and the modes were strong in the central region as well as the edges.

The method used in this work of coating microspheres with silicon nanocrystals

has demonstrated higher Q factors than those for planar microcavities containing silicon nanocrystals. Quality factors of up to 1500 were observed for individual modes, and this value may have been limited by the spectrometer resolution. The Q factor increased with sphere size (the highest Q was measured from nominally 20 μm diameter spheres), as expected by theoretical predictions [34]. The thickness of the nanocrystal film was also shown to be related to Q factor. Q increased with decreasing film thickness since the added volume represented an effective deformation of the sphere and therefore a loss of mode structure. Other factors that may have decreased Q were microdust particles and water vapor on the surface, surface defects or roughness of the spheres, and the roughness of the film itself. As well, the size distribution of the spheres lowered the Q factor of an ensemble of spheres compared to the Q factor of a single isolated sphere.

This method can be improved by several slight alterations which are known to increase Q factors: using larger spheres, using spheres with a higher refractive index, keeping the samples very clean (ex. preparing and storing them in special chambers), chemically treating the samples to avoid surface hydration, or preparing smoother films by using a different evaporation method (eg. thermal evaporation). However, the method is limited for two reasons. The first is that the spheres are not uniformly coated with the nanocrystal film and this seriously limits the Q factor. For very high Q factors, the films will have to be uniform around the entire sphere so as not to alter its shape. The second limitation, in terms of potential applications, is that it is not an easy task to produce the samples. A new method should address both of these issues.

In the future, our group plans to investigate the possibility of using chemical methods to uniformly coat the microspheres with SRO. This should produce higher Q factors by maintaining sphericity. Also, as shown in the theory section of this thesis, maximum Q factors are obtained from such structures when the nanocrystals are near the sphere surface.

Microlasers have been developed in the past by trapping the light from direct gap semiconductors into the WGMs of a microsphere [47, 76]. This author predicts that with some clever ideas and experimentation in the future, the same can be achieved using silicon nanocrystals and microspheres.

Bibliography

[1] World record for silicon light emission. *III-Vs Review The Advanced Semiconductor Magazine*, 16(1):25, 2003.

[2] M. Ajgaonkar, Y. Zhang, H. Grebel, and C. White. Nonlinear optical properties of a coherent array of submicron SiO_2 spheres (opal) embedded with Si nanoparticles. *Applied Physics Letters*, 75(11):1532, 1999.

[3] A. Alivisatos. Semiconductor clusters, nanocrystals, and quantum dots. *Science*, 271:933, 1996.

[4] N. Anscombe. Efficient silicon LED demonstrated. *Photonics Spectra*, January 2003.

[5] M. Artemyev and U. Woggon. Quantum dots in photonic dots. *Applied Physics Letters*, 76(11):1353, 2000.

[6] M. Artemyev, U. Woggon, and W. Langbein. Quantum dot emission confined by a spherical photonic dot. *Physica Status Solidi (b)*, 229(1):423, 2002.

[7] M. Artemyev, U. Woggon, R. Wannemacher, H. Jaschinski, and W. Langbein. Light trapped in a photonic dot: Microspheres act as a cavity for quantum dot emission. *Nano Letters*, 1(6):309, 2001.

[8] A. Beltaos and A. Meldrum. Whispering gallery modes in silicon-nanocrystal coated silica microspheres. To be submitted to the *Journal of Luminescence*, April 2006.

[9] S. Brorson and P. Skovgaard. *Optical Processes in Microcavities*, chapter 2: Optical mode density and spontaneous emission in microcvaities, page 77. World Scientific, New Jersey, 1998.

[10] M. Cai, O. Painter, J. Vahala, and P. Sercel. Fiber-coupled microsphere laser. *Optics Letters*, 25(19):1430, 2000.

[11] P. Calcott, K. Nash, L. Canham, M. Kane, and D. Brumhead. Identification of radiative transitions in highly porous silicon. *Journal of Physics: Condensed Matter*, 5:L91, 1993.

[12] L. Canham. Silicon quantum wire array fabrication by electrochemical and chemical dissolution of wafers. *Applied Physics Letters*, 57(10):1046, 1990.

[13] R. Carius, R. Fischer, E. Holzenkämpfer, and J. Stuke. Photoluminescence in the amorphous system SiO_x. *Journal of Applied Physics*, 52:4241, 1981.

[14] H. Chew. Transition rates of atoms near spherical surfaces. *Journal of Chemical Physics*, 87(2):1355, 1987.

[15] H. Chew. Radiation and lifetimes of atoms inside dielectric particles. *Physical Review A*, 38(7):3410, 1988.

[16] H. Chew, P. McNulty, and M. Kerker. Model for raman and fluorescent scattering by molecules embedded in small particles. *Physical Review A*, 13(1):396, 1976.

[17] S. Ching, H. Lai, and K. Young. Dielectric microspheres as optical cavities: Einstein a and b coefficients and level shift. *Journal of the Optical Society of America B*, 4(2004), 1987.

[18] S. Ching, H. Lai, and K. Young. Dielectric microspheres as optical cavities: thermal spectrum and density of states. *Journal of the Optical Society of America B*, 4:1995, 1987.

[19] T. Clement. Optical microcavities with source applications. Final report for ECE 685: Photonic devices, The Univeristy of Alberta, 2003.

[20] L. Collot, V. Lefèvre-Seguin, M. Brune, J. Raimond, and S. Haroche. Very high-Q whispering gallery mode resonances observed on fused silica microspheres. *Europhysics Letters*, 23(5):327, 1993.

[21] C. Delerue, G. Allan, and M. Lannoo. Theoretical aspects of the luminescence of porous silicon. *Physical Review B*, 48:11024, 1993.

[22] C. Delerue, G. Allan, and M. Lannoo. Optical band gap of Si nanoclusters. *Journal of Luminescence*, 80:65, 1999.

[23] C. Delerue, G. Allan, and M. Lannoo. Electron-phonon coupling and optical transitions for indirect-gap semiconductor nanocrystals. *Physical Review B*, 64:193402.1, 2001.

[24] A. Efros and A. Efros. Pioneering effort I. *Sov. Phys. Semicond.*, 16:772, 1982.

[25] S. Furukawa and T. Miyasato. Quantum size effects on the optical band gap of microcrystalline Si:H. *Physical Review B*, 38:5726, 1988.

[26] S. Gaponenko. *Optical Properties of Semiconductor Nanocrystals.* Cambridge University Press, 1998.

[27] M. Glover. Photoluminescence of silicon nanocrystal superlattices. Master's thesis, The University of Alberta, 2005.

[28] M. Glover and A. Meldrum. Effect of buffer layers on the optical properties of silicon nanocrystal superlattices. *Optical Materials*, 27:977, 2005.

[29] F. Gorbilleau, X. Portier, C. Ternon, P. Voivenel, R. Madelon, and R. Riszk. Si-rich/SiO_2 nanostructured multilayers by reactive magnetron sputtering. *Applied Physics Letters*, 78:3058, 2001.

[30] M. Gorodetsky, A. Savchenkov, and V. Ilchenko. Ultimate Q of optical microsphere resonators. *Optics Letters*, 21(7):453, 1996.

[31] M. Han, X. Gao, J. Su, and S. Nie. Quantum-dot-tagged microbeads for multiplexed optical coding of biomolecules. *Nature Biotechnology*, 19:631, 2001.

[32] N. Hill and K. Whaley. Size dependence of excitons in silicon nanocrystals. *Physical Review Letters*, 75:1130, 1995.

[33] N. Hill and K. Whaley. A theoretical study of light emission from nanoscale silicon. *Journal of Electronic Materials*, 25:269, 1996.

[34] S. Hill and R. Benner. *Optical Effects Associated with Small Particles*, chapter 1: Morphology-Dependent Resonances, page 3. World Scientific, 1988.

[35] A. Hryciw, K. Buchanan, A. Meldrum, and C. White. Effects of particle size and excitation spectrum on the photoluminescence of silicon nanocrystals formed by ion implantation. *Nuclear Instruments and Methods in Physics Research Section B: Beam Interactions with Materials and Atoms*, 222:469, 2004.

[36] A. Hryciw, J. Laforge, C. Blois, M. Glover, and A. Meldrum. Tunable luminescence from a silicon-rich oxide microresonator. *Advanced Materials*, 17(7):845, 2005.

[37] F. Huiskin, D. Amans, G. Ledoux, H. Hofmeister, F. Cichos, and J. Martin. Nanostructuration with visible-light-emitting silicon nanocrystals. *New Journal of Physics*, 5:10.1, 2003.

[38] M. Hybertson. Absorption and emission of light in nanoscale silicon structures. *Physical Review Letters*, 72(10):1514, 1994.

[39] F. Iacona, G. Franzò, E. Ceretta Moreira, D. Pacifici, A. Irrera, and F. Priolo. Luminescence properties of Si nanocrystals embedded in optical microcavities. *Materials Science and Engineering C*, 19:377, 2002.

[40] F. Iacona, G. Franzò, E. Moreira, and F. Priolo. Silicon nanocrystals and Er^{3+} ions in an optical microcavity. *Journal of Applied Physics*, 89(12):8354, 2001.

[41] R. Jia, D. Jiang, P. Tan, and B. Sun. Quantum dots in glass spherical microcavity. *Applied Physics Letters*, 79(2):153, 2001.

[42] J. Joannopoulos, R. Meade, and J. Winn. *Photonic Crystals*. Princeton University Press, 1995.

[43] U. Kahler and H. Hofmeister. Visible light emission from Si nanocrystalline composites via reactive evaporation of SiO. *Optical Materials*, 17:83, 2001.

[44] U. Kahler and H. Hofmeister. Visible light emission from Si nanocrystalline composites via reactive evaporation of SiO. *Optical Materials*, 17:8, 2001.

[45] S. Kasap. *Optoelectronics and Photonics: Principles and Practices.* Prentice Hall, 2001.

[46] V. Klimov. Nanocrystal quantum dots. *Los Alamos Science*, (28):214, 2003.

[47] V. Klimov and M. Bawendi. Ultrafast carrier dynamics, optical amplification, and lasing in nanocrystal quantum dots. *MRS Bulletin*, page 998, 2001.

[48] V. Klimov, Ch. Schwarz, D. McBranch, and C. White. Initial carrier relaxation dynamics in ion-implanted Si nanocrystals: Femtosecond transient absorption study. *Applied Physics Letters*, 73:2603, 1998.

[49] W. Klitzing, R. Long, V. Ilchenko, J. Hare, and V. Lefèvre-Seguin. Tunable whispering gallery modes for spectroscopy and CQED experiments. *New Journal of Physics*, 3:14.1, 2001.

[50] D. Kovalev, J. Diener, H. Heckler, G. Polisski, N. Künzner, and F. Koch. Optical absorption cross sections of Si nanocrystals. *Physical Review B*, 61(7):4485, 2000.

[51] D. Kovalev, H. Heckler, M. Ben-Charin, G. Polisski, M. Schwartzkopff, and F. Koch. Breakdown of the k-conservation rule in Si-nanocrystals. *Physical Review Letters*, 81:2803, 1998.

[52] D. Kovalev, H. Heckler, G. Polisski, J. Diener, and F. Koch. Optical properties of silicon nanocrystals. *Optical Materials*, 17:35, 2001.

[53] S. Lacey and H. Wang. Directional emission from whispering-gallery modes in deformed fused-silica microspheres. *Optics Letters*, 26(24):1943, 2001.

[54] C. Lam, P. Leung, and K. Young. Explicit asymptotic formulas for the positions, widths, and strengths of resonances in Mie scattering. *Optical Society of America B*, 9(9):1585, 1992.

[55] V. Lefèvre-Seguin. Whispering gallery mode lasers with doped silica microspheres. *Optical Materials*, 11:153, 1999.

[56] M. López, B. Garrido, C. Bonafos, A. Pérez-Rodríguez, J. Morante, and A. Claverie. Model for efficient visible emission from Si nanocrystals ion beam

synthesized in SiO_2. *Nuclear Instruments and Methods in Physics Research B*, 178:89, 2001.

[57] M. López, B. Garrido, C. Garcia, P. Pellegrino, A. Pérez-Rodríguez, J. Morante, C. Bonafos, M. Carrada, and A. Claverie. Elucidation of the surface passivation role on the photoluminescence emission yield of silicon nanocrystals embedded in SiO_2. *Applied Physics Letters*, 80:1637, 2002.

[58] B. Lu, Y. Wang, Y. Li, and Y. Liu. Cavity-modified spontaneous emission rate in Nd-glass microsphere. *SPIE*, 1979:166, 1992.

[59] A. Meldrum. Optical properties of silicon nanocrystals. *Recent Research Developments in Nuclear Physics*, 1:93, 2004.

[60] A. Meldrum, R. Haglund, L. Boatner, and C. White. Nanocomposite materials formed by ion implantation. *Advanced Materials*, 13:1431, 2001.

[61] A. Meldrum, A. Hryciw, K. Buchanan, A. Beltaos, M. Glover, C. Ryan, and J. Veinot. Two-dimensionally-patterned silicon nanocrystal arrays. *Optical Materials*, 27(5):812, 2005.

[62] C. Murphy and J. Coffer. Quantum dots: A primer. *Applied Spectroscopy*, 56(1):16A, 2002.

[63] E. Neufeld, S. Wang, R. Apetz, Ch. Buchal, R. Carius, C. White, and D. Thomas. Effect of annealing and H_2 passivation on the photoluminescence of Si nanocrystals in SiO_2. *Thin Solid Films*, 294:238, 1997.

[64] S. Ögüt, J. Chelikowski, and S. Louie. Quantum confinement and optical gaps in Si nanocrystals. *Physical Review Letters*, 79:1770, 1997.

[65] L. Pavesi, C. Mazzoleni, C. Tredicucci, and V. Pelligrini. Controlled photon emission in porous silicon microcavities. *Applied Physics Letters*, 67(22):3280, 1995.

[66] M. Pelton and Y. Yamamoto. Ultralow threshold laser using a single quantum dot and a microsphere cavity. *Physical Review A*, 59(3):2418, 1999.

[67] E. Peter, P. Senellart, D. Martrou, A. Lemaître, J. Hours, J. Gérard, and J. Bloch. Exciton-photon strong-coupling regime for a single quantum dot embedded in a microcavity. *Physical Review Letters*, 95:067401–1, 2005.

[68] C. Pickering, M. Beale, D. Robbins, P. Pearson, and R. Greef. Optical studies of the structure of porous silicon films formed in p-type degenerate and non-degenerate silicon. *Journal of Physics C: Solid State Phys.*, 17:6535, 1984.

[69] E. Purcell. Spontaneous emission probabilities at radio frequencies. *Physical Review*, 69:681, 1946.

[70] C. Ryan, A. Meldrum, and C. White. Luminescence and microstructure of microspheres containing silicon nanocrystals. *Materials Research Society Symp. Proc.*, 703:21, 2003.

[71] S. Schiller. Asymptotic expansion of morphological resonance frequencies in Mie scattering. *Applied Optics*, 32(12):2181, 1993.

[72] S. Schiller and R. Byer. High-resolution spectroscopy of whispering gallery modes in large dielectric spheres. *Optics Letters*, 16(15):1138, 1991.

[73] H. Schniepp and V. Sandoghar. Spontaneous emission of europium ions embedded in dielectric nanospheres. *Physical Review Letters*, 89(25):257403–1, 2002.

[74] N. Sharma, V. Keast, T. Iwayama, I. Boyd, and C. Humphreys. Characterisation of silicon nanocrystals in silica and correlation with luminescence. *Electron Microscopy and Analysis*, 161:589, 1999.

[75] T. Shimizu-Iwayama, M. Ohshima, T. Niimi, S. Nakao, K. Saitoh, T. Fujita, and N. Itoh. Visible photoluminescence related to Si precipitates in Si^+-implanted SiO_2. *J. Phys.: Condens. Matter*, 5:L375, 1993.

[76] P. Snee, Y. Chan, D. Nocera, and M. Bawendi. Whispering-gallery-mode lasing from a semiconductor nanocrystal/microsphere resonator composite. *Advanced Materials*, 17:1131, 2005.

[77] S. Spillane. *Fiber-coupled Ultra-high-Q Microresonators for Nonlinear and Quantum Optics*. PhD thesis, California Institute of Technology, 2004.

[78] K. Toshikiyo, M. Fujii, and S. Hayashi. Enhanced optical properties of Si nanocrystals in planar microcavity. *Physica E*, 17:451, 2003.

[79] T. Trupke, J. Zhao, A. Wang, R. Corkish, and M. Green. Very efficient light emission from bulk crystalline silicon. *Applied Physics Letters*, 82(18):2996, 2003.

[80] K. Vahala. Optical microcavities. *Nature*, 424, 2003.

[81] J. Valenta, J. Dian, K. Luterová, P. Knápek, I. Pelant, M. Nikl, D. Muller, J. Grob, J. Rehspringer, and B. Hönerlage. Temperature behaviour of optical properties of Si^{+}-implanted SiO_2. *European Physics Journal D*, 8:395, 2000.

[82] J. Valenta, J. Linnros, R. Juhasz, J. Rehspringer, F. Huber, C. Hirlimann, Cheylan S., and R. Elliman. Photonic band-gap effects on photoluminescence of silicon nanocrystals embedded in artifical opals. *Journal of Applied Physics*, 93(8):4471, 2003.

[83] I. Vasiliev, J. Chelikowski, and R. Martin. Surface oxidation effects on the optical properties of silicon nanocrystals. *Physical Review B*, 65:121302, 2002.

[84] J. Veinot, H. Yan, S. Smith, J. Cui, Q. Huang, and T. Marks. Fabrication and properties of organic light-emitting nanodiode arrays. *Nano Letters*, 2(4):333, 2002.

[85] D. Vernooy, V. Ilchenko, H. Mabuchi, E. Streed, and H. Kimble. High-Q measurements of fused-silica microspheres in the near infrared. *Optics Letters*, 23(4):247, 1998.

[86] V. Vinciguerra, G. Franzò, F. Priolo, F. Iacona, and C. Spinella. Quantum confinement and recombination dynamics in silicon nanocrystals embedded in Si/SiO_2 superlattices. *Journal of Applied Physics*, 87:8165, 2000.

[87] L. Wang and A. Zunger. Electronic structure pseudopotential calculations of large (.apprx.1000 atoms) Si quantum dots. *Journal of Physical Chemistry*, 98:2158, 1994.

[88] Y. Wang, B. Lu, Y. Li, and Y. Liu. Observation of cavity quantum-electrodynamic effects in a Nd: glass microsphere. *Optics Letters*, 20(7):770, 1995.

[89] J. Wilcoxon, G. Samara, and P. Provencio. Optical and electronic properties of Si nanoclusters synthesized in inverse micelles. *Physical Review B*, 60:2704, 1999.

[90] S. Withrow, C. White, A. Meldrum, and J. Budai. Effects of hydrogen in the annealing environment on photoluminescence from Si nanoparticles in SiO_2. *Journal of Applied Physics*, 86:396, 1999.

[91] U. Woggon, R. Wannemacher, M. Artemyev, B. Möller, N. Lethomas, V. Anikeyev, and O. Schöps. Dot-in-a-dot: Electronic and photonic confinement in all three dimensions. *Applied Physics B*, 77:469, 2003.

[92] D. Wolford, J. Reimer, and B. Scott. Efficient visible photoluminescence in the binary a-Si:H_x alloy system. *Applied Physics Letters*, 42:369, 1983.

[93] M. Wolkin, P. Fauchet, G. Allan, and C. Delerue. Electronic states and luminescence in porous silicon quantum dots: The role of oxygen. *Physical Review Letters*, 82:197, 1999.

[94] Y. Yamamoto and R. Slusher. Optical processes in microcavities. *Physics Today*, page 66, 1993.

[95] T. Yamasaki and T. Tsutsui. Fabrication and optical properties of two-dimensional ordered arrays of silica microspheres. *Japanese Journal of Applied Physics*, 38(10):5916, 1999.

[96] Y. Zhang, S. Vijayalakshmi, M. Ajgaonkar, H. Grebel, and C. White. Optical properties of an ordered array of silica nanospheres embedded with silicon nanoclusters. *Journal of the Optical Society of America B*, 17(12):1967, 2000.

Appendix

The following text is the program written in Matlab to calculate Mie resonance locations according to reference [71]. The expression "..." is used at the end and beginning of a line to indicate that the text should continue in a single line in Matlab. The actual "..." should be removed from the text when inserting the code into Matlab.

```
% Mie.m written by Angela Beltaos and Aaron Hryciw
% following Schiller, Appl. Opt. vol. 32., No.12 (1993)

function mie=x(n,l,pol,m)

% X = MIE(n,l,pol,m) returns the size parameter x(n,l) where:
% n = angular mode number
% l = radial mode number
% pol = "'TE'" or "'TM'"
% m = relative refractive index of sphere to surrounding medium


if (pol=='TM'|pol=='tm')
    p=1/m^2;
    w=1;
else p=1;
     w=0;
end  % Default is TE
```

```
% Roots of the lth Airy functions, ail(l) are according to Lam et
al., Opt. Soc. Am. B, vol. 9, No. 9, (1992).
ail=-[2.338 4.088 5.521 6.787 7.944 9.023 10.040 11.009 11.936...
... 12.829 13.692 14.528 15.341 16.133 16.906];   % Airy fcn roots

v=n+1/2;

% Define ep (e prime)

ep=[0
    0
    0
    (-8+12*m^4+m^8)/m^8   % e4'
    7000*m^-6*(-28-m^2+56*m^4-16*m^6-7*m^8+2*m^10)   % e5'
    m^-8*(5*(-200-32*m^2+526*m^4-226*m^6-99*m^8+62*m^10+4...
    ...*m^12)+2*(-400+272*m^2+744*m^4-424*m^6-366*m^8-2*m^...
    ...10+m^12)*ail(l)^3) %e6'
    -269500*m^-8*(-232+160*m^2+543*m^4-447*m^6-186*m^8+165...
    ...*m^10-15*m^12+4*m^14) %e7'
    m^-10*ail(l)*(-10*(-459200+286000*m^2+1360312*m^4-...
    ...1305476*m^6-433952*m^8+717562*m^10-209039*m^12-21542...
    ...*m^14+7060*m^16)+3*(336000-441600*m^2-626496*m^4+...
    ...891008*m^6+306416*m^8-505696*m^10-72488*m^12-7664*m...
    ...^14+2395*m^16)*ail(l)^3) %e8'
    ];

e=w*(m^2-1)*ep;

% Define d (dk)

d=[-p                                          %d0
   2^(1/3)*3*(m^2-1)*ail(l)^2/(20*m)           %d1
```

```
  -2^(2/3)*m^2*p*(-3+2*p^2)*ail(1)/6            %d2
  (350*m^4*(1-p)*p*(-1+p+p^2)+(m^2-1)^2*(10+ail(1)^3))/...
  ...(700*m)   %d3
  -2^(1/3)*m^2*ail(1)^2*(4-m^2+e(4))/20              %d4
  ail(1)*(40*(-1+3*m^2-3*m^4+351*m^6)-479*(m^2-1)^3*ail(1)...
  ...^3-e(5))/(2^(4/3)*63000*m)   %d5
  (5*m^2*(-13-16*m^2+4*m^4)+2*m^2*(128-4*m^2+m^4)*ail(1)^3...
  ...-e(6))/1400              %d6
  ail(1)^2*(100*(-551+2204*m^2-3306*m^4-73256*m^6+10229*m^...
  ...8)-20231*(m^2-1)^4*ail(1)^3+e(7))/(2^(2/3)*16170000*m)   %d7
  (m^2*ail(1)*(10*(11082+44271*m^2-288*m^4+7060*m^6)-3*(52544...
  ...+48432*m^2-11496*m^4+2395*m^6)*ail(1)^3)+e(8))/(2^(10/3)...
  ...*141750)  %d8
  ];

sumdk=0;

for k=0:8
    sumdk=sumdk+(d(k+1)./(v.^(k/3)*(m^2-1)^((k+1)/2)));
end

xnl=v/m-ail(1)/m*(v/2).^(1/3)+sumdk; x=xnl
```